This is a preprint, the final version is subject to change, of the American Mineralogist (MSA)
Cite as Authors (Year) Title. American Mineralogist, in press.
DOI: https://doi.org/10.2138/am-2020-7021

Revision 1

New insights into the evolution of MVT hydrothermal system: A case study of the Wusihe Pb-Zn deposit (South China), using quartz in situ trace elements and sulfides in situ S-Pb isotopes

KAI LUO[1,2,4], JIA-XI ZHOU[1,3,4,*], ZHI-LONG HUANG[1], JOHN CAULFIELD[4], JIAN-XIN ZHAO[4], YUE-XING FENG[4], HEGEN OUYANG[4,5]

[1] *State Key Laboratory of Ore Deposit Geochemistry, Institute of Geochemistry, Chinese Academy of Sciences, Guiyang 550081, China*

[2] *University of Chinese Academy of Sciences, Beijing 100049, China*

[3] *School of Resource Environment and Earth Sciences, Yunnan University, Kunming 650500, China*

[4] *School of Earth and Environmental Sciences, The University of Queensland, Brisbane QLD 4072, Australia*

[5] *Key Laboratory of Metallogeny and Mineral Assessment, Institute of Mineral Resources, Chinese Academy of Geological Sciences, Beijing, 100037, China*

*Corresponding author, JIA-XI ZHOU, E-mail, zhoujiaxi@ynu.edu.cn

ABSTRACT

Unraveling the evolution of MVT hydrothermal system is crucial for understanding ore genesis and exploration. In this paper, we take the Wusihe Pb-Zn deposit in the western Yangtze Block (South China) as a case study, using detailed ore deposit geology, quartz in situ trace elements and sulfides in situ S-Pb isotopes, to propose a new integrated model for the evolution of MVT hydrothermal system. Four hydrothermal stages were identified in the Wusihe ore district: (I) lamellar pyrite-sphalerite; (II) disseminated, stock-work and brecciated sphalerite-galena; (III) massive galena, and (IV) veined calcite-bitumen. Within the most representative stage (stage-II), Al concentrations increase from 8.46-354 ppm (mean 134 ppm) of Q1 to 171-3049 ppm (mean 1062 ppm) of Q2, and then decrease to 3.18-149 ppm (mean 25.4 ppm) of Q3. This trend indicates the role of acid-producing processes that resulted from sulfide precipitation, and acid consumption by carbonate buffering. The occurrence of authigenic non-altered K-feldspar provides further evidence that the ore-forming fluids were weakly acidic with pH values of > ~5.5. Moreover, new bulk $\delta^{34}S$ values of sulfides (+1.8-+14.3‰) are overall lower than those previously reported (+7.1-+20.9‰), implying that in addition to thermochemical sulfate reduction (TSR), bacterial sulfate reduction (BSR) may also play an important role in the formation of S^{2-}. In situ $\delta^{34}S$ values show a larger range (-4.3-+26.6‰), and significantly, varies within

This is a preprint, the final version is subject to change, of the American Mineralogist (MSA)
Cite as Authors (Year) Title. American Mineralogist, in press.
DOI: https://doi.org/10.2138/am-2020-7021

single grains (up to +12.3‰), suggesting mixing of two isotopically distinct S^{2-} end-members produced by TSR and BSR. The diagenetic and hydrothermal early phase (stage-I) sulfides were formed within a nearly closed system of BSR, whereas the formation of late phase (stages-II and -III) sulfides was caused by the input of hydrothermal fluids that promoted TSR. New galena in situ Pb isotopic ratios ($^{206}Pb/^{204}Pb$ = 18.02-18.19, $^{207}Pb/^{204}Pb$ = 15.66-15.69 and $^{208}Pb/^{204}Pb$ = 38.14-38.39) suggest that the sources of mineralizing metals in the Wusihe deposit are mainly Proterozoic basement rocks. Hence, a multi-process model (i.e. basin-mountain coupling, fluid mixing, local sulfate reduction, in situ acid-producing and involvement of black shales and carbonate sequences) was responsible for the formation of the Wusihe deposit, whilst S^{2-} was produced by both TSR and BSR, providing new insights into the evolution of MVT hydrothermal system.

Keywords: Quartz in situ trace elements; Sulfides in situ S-Pb isotopes; MVT hydrothermal system evolution; Wusihe Pb-Zn deposit, South China

INTRODUCTION

Mississippi Valley-type (MVT) deposits are named after classic districts located in the drainage basin of the Mississippi River in the central United States (Guilbert and Park 1986). These deposits can form by mixing of basinal fluids of contrasting reduced sulfur and metal content, driven by gravity or tectonic stress from an adjacent orogenic belt (e.g. Durham 1966; Appold and Garven 1999; Bradley and Leach 2003). Despite a broad consensus on this model for MVT ore genesis, there are a number of questions that remain unanswered (e.g. Leach et al. 2005, 2010; Huston et al. 2006). One such question is how to establish a complete evolution of an MVT hydrothermal system involving the original sulfur/metal source(s), detailed constraints on acid-producing processes, and precipitation models. The other is how to explain the absence of deposits in many basins that otherwise have very similar geological histories as well-endowed basins (Wilkinson 2013), namely what role the ore-forming environments (i.e. tectonic setting, wall rock sequences) played during Pb-Zn mineralization.

The Upper Yangtze Pb-Zn metallogenic province covers an area of 170,000 km^2 and contains approx. 400 carbonate-hosted epigenetic Pb-Zn deposits totaling ~26 Mt of metal reserves (Fig. 1; e.g. Liu 1999; Zhou et al. 2014a, 2018a). The Wusihe Pb-Zn deposit is the largest in the northwest part of the province (~5.4Mt grading 8.6% wt. Zn and 2.0 wt. % Pb) (Xiong et al. 2018).

This deposit is hosted in siliceous and evaporitic carbonate sequences of the late Ediacaran Dengying Formation, which are unconformably overlain by the early Cambrian Qiongzhusi Formation black shales (Shao and Li 1996; Xiong et al. 2018; Zhu et al. 2018). Despite the Wusihe deposit resembling MVT deposits in the central United States (Table S1; e.g. Wu et al. 2013; Xiong et al. 2018), it shows many distinctive geological and geochemical features that warrant further investigation (Table S1). Firstly, the Wusihe ore district is characterized by a ~50km length of ore-bearing strata (Lin 2005; Li 2007), which are clearly distinct from those of classical MVT deposits; Secondly, large amounts of bitumen and authigenic non-altered K-feldspar have been noted in association with the Pb-Zn mineralization; And lastly, the ore structures within this single deposit are very complex, including lamellar, stock-work, brecciated, veined, disseminated and massive ore types (Sverjensky 1981; Gibbins 1983).

Given these features, it has been proposed that the Wusihe deposit may have formed in a unique tectonic environment (Leach et al. 2005), which represents an ideal locality to investigate the interplay amongst these factors and the evolution of MVT hydrothermal system. Accordingly, to better understand how these aspects influenced Pb-Zn mineralization, we undertook a detailed research program to trace the ore formation processes.

Sulfur (S) and lead (Pb) isotopes are powerful indices that can be used to trace the sources of fluids and mechanism of sulfide precipitation (e.g. Ohmoto

100 1986; Wilkinson et al. 2005). High spatial resolution in situ S and Pb isotopic
101 measurements can provide vital information about the fluid origin and the
102 nature of mineralization processes, constraints that cannot be resolved using
103 conventional bulk analytical methods (Peevler et al. 2003; Kucha 2010; Xue et
104 al. 2015; Zhou et al. 2018b). Furthermore, aluminum (Al) concentrations in
105 quartz can be an effective proxy for the pH of ore-forming fluids, because they
106 are strongly affected by Al solubility (Rusk et al. 2008; Chen et al. 2011).
107 Using Scanning Electron Microscope Cathodoluminesence (SEM-CL),
108 Laser Ablation Inductively Coupled Plasma Mass Spectrometry (LA-ICPMS)
109 quartz in situ element analysis, bulk and Nano Secondary Ion Mass
110 Spectrometry (NanoSIMS) sulfide in situ S isotope analysis, and femtosecond
111 LA-Multi-collector ICPMS (LA-MC-ICPMS) galena in situ Pb isotope analysis,
112 this study aims to: i) evaluate the ore-forming tectonic settings and wall rock
113 sequences; ii) trace the nature of ore-forming fluids and sulfide precipitation
114 mechanisms; iii) investigate the evolution of the Wusihe MVT hydrothermal
115 system. The outcomes will contribute to a better understanding of the
116 formation of carbonate-hosted epigenetic Pb-Zn deposits surrounding the
117 Yangtze Block, and similar deposits globally.
118

119 **REGIONAL GEOLOGY**

120 The South China Block is made up of the Yangtze Block to the northwest

This is a preprint, the final version is subject to change, of the American Mineralogist (MSA)
Cite as Authors (Year) Title. American Mineralogist, in press.
DOI: https://doi.org/10.2138/am-2020-7021

and the Cathaysia Block to the southeast. The Yangtze and Cathaysia blocks were amalgamated along the Jiangnan Orogenic belt at around 820-850 Ma (Fig. 1; e.g. Zhou et al. 2009; Wang et al. 2010; Zhao et al. 2011; Zhao 2015; Wu et al. 2018). The collision of the South China Block with the North China Craton to the north and the Indochina Block to the south occurred during the Triassic (e.g. Hou et al. 2003; Li et al. 2014; Mi et al. 2015).

The Yangtze Block consists of Mesoproterozoic basement (Fig. 1b) overlain by Neoproterozoic to Cenozoic cover sequences (Zhou et al. 2002, 2006; Zhao et al. 2010). Mesoproterozoic folded basement rocks include the ~1.7 Ga Dongchuan and ~1.1 Ga Kunyang Groups and equivalents that mainly consist of greywackes, slates and other carbonaceous to siliceous sedimentary rocks surrounding the Yangtze Block (Wang et al. 2012). These rocks are unconformably overlain by shallow marine Paleozoic and Early Mesozoic cover sequences. Jurassic to Cenozoic strata are composed exclusively of continental sequences.

There are numerous MVT Pb-Zn districts surrounding the margin of the Yangtze Block, which are tectonically linked to basin deformation in response to orogenic activity (Fig. 1b; Wang et al. 2014). Along the identified basin-mountain margins of the Yangtze Block, the early Paleozoic Qinling-Dabie basin-mountain system in the north (e.g. Lu et al. 2003; Zhang et al. 2006; Jiang et al. 2010; Wang et al. 2010) hosts the ca. 486 Ma Mayuan

and ca. 434-406 Ma Shennongjia Pb-Zn deposits (Fig. 1b; e.g. Wang et al. 2008). The Jiangnan Orogenic Belt was active ca. 411-412Ma on the southeast margin of the Yangtze Block (Fig. 1b; e.g. Chu et al. 2012), which consists of the Qiandong-Xiangxi-E'xi basin-mountain system, and hosts the ca. 412 Ma Huayuan Pb-Zn district (Fig. 1b; e.g. Duan et al. 2014). Within the western margin of the Yangtze Block, the composite tectonic setting, i.e. the Xiaojiang thrust-fold, the Longmenshan intracontinental Orogenic Belt and Chuxiong foreland basins, hosts the Upper Yangtze Pb-Zn metallogenic province (Fig. 1b; Liu and Lin 1999; Zhou et al. 2013a, 2018a; Huang et al. 2010; Hu et al. 2017). This province contains ca. 362-411Ma (e.g. Wu 2013; Zhang et al. 2014; Xiong et al. 2018) and ca. 192-226Ma (e.g. Zhou et al. 2013b, 2015, 2018a and references therein) Pb-Zn deposits hosted in late Ediacaran to late Permian carbonate rocks (Zhou et al. 2018b). These two age clusters correspond to the orogenic events by collision compression and post-collisional extension during late Caledonian-early Variscan (Devonian) and late Indosinian-early Yanshanian (Triassic-Jurassic), respectively (e.g. Li et al. 2006; Shu 2006).

DEPOSIT GEOLOGY

Pb-Zn deposits within the Wusihe district in the north of the Upper Yangtze Pb-Zn metallogenic province include the Heiqu-Xuequ, Hetaoping, Niuxinshan

and Wusihe deposits, all of which are hosted in late Ediacaran-early Cambrian carbonate sequences. These deposits form a large metallogenic belt along the Dadu River Valley with a length of over 50km (Fig. 2a). Among these Pb-Zn deposits, Wusihe is the largest.

Strata

Exposed strata in the Wusihe district include Mesoproterozoic metamorphic basement and Neoproterozoic cover. The Mesoproterozoic metamorphic basement (namely the Ebian Formation) consists primarily of phyllite and is unconformably overlain by Neoproterozoic strata comprising three formations: Suxiong, Guanyinya, and Dengying. The Suxiong Formation represents a volcanic sequence containing pyroclastic deposits, tuff, and rhyolite. The Suxiong Formation is overlain by the Guanyinya Formation which is composed of shale, limestone, and dolomite. The Neoproterozoic Dengying Formation is the most important ore-hosting unit and consists of thickly-bedded cherty dolostone, with minor shales and thin (<1 m) phosphorite beds. The Lower Cambrian Qiongzusi Formation consists mainly of organic-rich black shales, and is a significant source of hydrocarbons (Fig. 2c; Huang et al. 2012).

Tectonics

Faults and folds are well developed in the Wusihe mining district. The principal faults are the NW-trending Matuo fault and the NE-trending Wangmaoshan fault. The main fold present is the Wanlicun syncline (Fig. 2a).

184 This tectonic framework produces secondary fault fracture zones and
185 interlayered fault zones, which control the spatial distribution of the stratiform
186 ore bodies.

187 **Ore bodies**

188 Ore bodies in the Wusihe deposit have variable thicknesses from 0.20-2.97
189 m, with a mean of 0.93 m. They are simple in shape, layered, extensively
190 lentoid, and dominantly occur parallel to wall rock bedding. Ore bodies contain
191 0.02-14.02 wt. % Pb (average 3.05 wt. %), and 0.58-37.60 wt. % Zn (average
192 12.4 wt. %), and can be divided into two groups: lower and upper. The lower
193 group of ore bodies is layered, and hosted in gray siliceous dolostones. This
194 group mainly contains sphalerite, characterized by lamellar ores with a minor
195 disseminated component. The upper group of ore bodies is hosted in
196 black-gray layered carbonaceous dolostone and minor black shales. The
197 upper group occurs as layered, lens shapes, up to 14m above the lower
198 boundary of the Qiongzhusi Formation black shale. They are 6.3-16.3m in
199 thickness (mean 12.3m), showing stock-work and disseminated ores in
200 interlayered crushed zones, dissolution collapse structures and brecciated
201 ores concentrated along fault planes.

202 **Mineralogy**

203 At Wusihe, ores are dominantly sulfides, with lesser amounts of oxides.
204 Mineral assemblages are comprised of both ore minerals including pyrite,

sphalerite and galena, along with gangue minerals including quartz, dolomite, calcite, bitumen and potassium feldspar (Figs. 3-5). Minerals display mainly granular and colloform textures. Field observations identified six different modes of occurrence of the Pb-Zn sulfide ores in the Wusihe deposit, including lamellar, disseminated, stock-work, brecciated, veined and massive (Fig. 3). According to the mineral assemblages and crosscutting relationships shown by the deposit, four stages of hydrothermal mineralization can be established (Fig. 6): Stage I: pyrite-sphalerite (nodules and bands of lamellar ore); Stage II: sphalerite-galena (disseminated, stockwork, brecciated ore); Stage III: galena (massive ore) and Stage IV: bitumen-calcite. The disposition of the various types of ores at Wusihe is shown schematically in Fig. 11b.

The lamellar ore typically consists of fine-grained sphalerite and pyrite horizons (several mm to cm in thickness) in carbonaceous-, siliceous-dolostone or black shales (Fig. 3a). This ore-type is characterized by rhythmic sulfide bands, comprising yellow, brown and red colored sphalerite (60–70%), pyrite (10–20%) and minor organic matter (<10%). Structurally these bands run parallel to bedding and schistosity in the siliceous dolostone.

The disseminated ore is comprised of fine- to coarse-grained sphalerite and pyrite (0.1mm-10mm). This type of ore often appears to be red-brown/light brown intergrown with light-yellow concentric rings (Fig. 3b-f). Quartz can be divided into three generations: the first generation (Q1) occurs as euhedral

hexagon grains (Fig. 5b). The second generation (Q2) is commonly subhedral coexisting with sulfides (Fig. 5c, d). The third generation (Q3) occurred as veinlets crosscutting sulfides or along the margins of dolomite (Fig. 5e, f).

The stock-work ore is composed of sphalerite and galena where sphalerite dominates (60-70%), followed by galena (10-20%), calcite (5-10%), quartz (1-3%) and occasional pyrite (Fig. 3g, h). Calcite is mainly dispersed as either blocks or short veins with a small number of occurrences along the margins of sphalerite veins (Fig. 4d, k). Quartz is dominantly distributed along the margins of sphalerite veins, and includes large amounts of irregular bitumen (Fig. 4k).

The brecciated ore consists of sphalerite and irregular galena aggregates (Fig. 3i, j). They form the cement matrix to early deformation lamellar ores hosted in the siliceous dolostone. These sphalerites are predominantly yellow in color, ellipsoidal in shape, and form parallel strips with a dominant grain size of 0.5-1.2 mm. In some cases, the sphalerite occurs as single and multi-colored concentric rings (Fig. 4e, f, g). Galena grains are almost square, dispersed in sphalerite grains and locally rims the sphalerite. Quartz grains are clear and coarse (0.02-0.1cm) (Fig. 4c, d).

The massive ore is the highest-grade ore-type in the Wusihe deposit. It occurs as massive lodes and ore shoots 0.5 to 3 m in width. Galena is well-formed and the dominant ore mineral (60-70%) followed by sphalerite (20-30%) and pyrite (10%) (Fig. 3k, l).

The late bitumen-carrying calcite occurs mainly as veins (Figs. 3c and 4d, k, l). The calcite veins contain small amounts of sphalerite and bitumen and partially cut early quartz veins (Fig. 3c). Quartz occurs as granular, partially fibrillar, or comb-like structures (Figs. 4c and 5e, f). Quartz grains are typically 0.05-0.2mm, occasionally reaching 0.5mm.

Alteration

Hydrothermal alteration at Wusihe primarily consists of silicification, pyritization and carbonatization. Alteration is mainly found in fault zones, and less commonly in the rocks hosting stratiform ore bodies. Silicification is the most pervasive alteration type in the Wusihe deposit. It mainly occurs as clear veinlets and lenses in the carbonates that are characterized by high permeability. Quartz occurs in vugs as subhedral-euhedral grains. The interior of quartz veinlets contains sphalerite and galena. Pyritization mainly occurs as irregular aggregates of fine-grained pyrite in the banded dolostone hosting lamellar ores, or disseminated pyrite intergrown with silicification or veinlets in carbonate breccias. Late, relatively weak carbonatization, is preserved as rare veinlets, and shows no genetic relationship with sulfides.

SAMPLING AND ANALYTICAL METHODS

This study employs surface geological mapping, drill core logging, petrographic observations, and geochemical and isotopic analyses. We

analyzed twenty-four single sulfide grains (0.4-1mm in size) separated from the ores and thirteen representative thin sections of the main mineralization stages. Twenty-four single sulfide grains were selected for bulk sulfur isotope analysis, using a Finnigan MAT-253 mass spectrometer at the State Key Laboratory of Ore Deposit Geochemistry, Institute of Geochemistry, Chinese Academy of Sciences (SKLODG-IGCAS). The precision calculated from replicated analysis of unknown samples was better than 0.2‰ (2σ). Five thin sections were imaged for SEM-CL, using JSM7800F SEM equipped with a Mono CL4 detector at the SKLODG-IGCAS. Two thin sections were selected for LA-ICPMS in situ trace element analysis of quartz from the most representative mineralization stage (stage-II). Analyses were conducted at the SKLODG-IGCAS, using an Agilent 7900 ICP-MS equipped with a GeoLasPro 193 nm ArF excimer laser. The uncertainties on Li, Na, Mg, Al, K, Ti and Ge measurements are less than 6%. Four thin sections were selected for NanoSIMS in situ analysis of S isotopes in pyrite and sphalerite. They were acquired on a CAMECA NanoSIMS 50 L at the Key Laboratory of Earth and Planetary Physics, Institute of Geology and Geophysics, CAS. The analytical precision calculated from replicated analysis of unknown samples is better than 0.2‰ (1s). Four thin sections were analyzed using a femtosecond LA-MC-ICPMS setup for in situ analysis of Pb isotopes in galena. The analyses were measured using a Nu II MC-ICP-MS (Nu Instruments, Wrexham,

289 UK) combined with a 193 nm RESOlution M-50 femtosecond (fs) laser ablation
290 system (ASI) at the State Key Laboratory of Continental Dynamics, Northwest
291 University, China. Repeated analyses of NIST SRM 610 glass standard
292 yielded highly reliable and reproducible results during the entire analytical
293 session with mean $^{206}Pb/^{204}Pb$, $^{207}Pb/^{204}Pb$ and $^{208}Pb/^{204}Pb$ ratios of 17.052 ±
294 0.003, 15.515 ± 0.003 and 36.980 ± 0.007 (1SD, n=183), respectively. Detailed
295 analytical methods for in situ quartz trace element analysis, bulk S and in situ
296 S-Pb isotopes are included in Appendix-1.
297
298 **RESULTS**
299 Stage-II is the most representative phase. Al concentrations increase from
300 8.46-354 ppm (mean 134 ppm; n=8) in Q1 to 171-3049 ppm (mean 1062ppm;
301 n=38) in Q2, and then decrease to 3.18-149 ppm (mean 25.4 ppm; n= 24)
302 (Table 2). Clear linear correlations are observed among Li, Na and K vs. Al
303 contents in quartz (Fig. 7a-c). The results of bulk sulfur isotope measurements
304 are summarized in Table 1 and are shown in Figs. 8a and 9b. Bulk $\delta^{34}S$ values
305 range from +1.8‰ to +14.3‰ (n=24). The overall range of in situ $\delta^{34}S$ values
306 at the micro-scale in pyrite and sphalerite grains is from -4.3‰ to +26.6‰,
307 which is larger than the range of bulk sulfides (+1.8-+14.2‰; Figs. 8b and 9a, c)
308 and include some of the lowest (negative) values ever reported. The in situ
309 $\delta^{34}S$ values of diagenetic pyrite vary from +23.4‰ to +24.4‰ (n=4), those of

stage-I sulfides range from +16.5‰ to +26.6‰ (n=12), and stage-II and -III range from +0.1-+11.8‰ (n=8) and -4.3-+12.3‰ (n=14), respectively. Galena in situ Pb isotopic ratios are presented in Table 4 and are shown in Fig. 11a-c. Galena grains have the following in situ Pb isotopic ratios: $^{206}Pb/^{204}Pb$ = 18.02-18.19, $^{207}Pb/^{204}Pb$ = 15.66-15.69 and $^{208}Pb/^{204}Pb$ = 38.14-38.39, with μ ($^{238}U/^{204}Pb$) values of 9.63-9.67 (n=36). Full details of in situ trace element data, bulk S, and in situ S and Pb isotopes are included in Appendix-2.

DISCUSSION

Acid-producing processes

The dark-grey Q1 quartz occurs as euhedral-subhedral grains, enclosed by Q2, which is characterized by euhedral oscillatory growth zones showing variable CL intensity. Q3 dark anhedral quartz veins cut the former two generations of quartz. These complex CL textures are considered to reflect the wide range of physical and chemical conditions under which hydrothermal quartz forms (Götze and Möckel 2012).

In quartz, compensated substitution ($Al^{3+}+H^{+}/Li^{+}/Na^{+}/K^{+}\rightarrow Si^{4+}$) is one of the key substitution modes governing the incorporation of structural trace elements (Mackey 1963; Götze et al. 2001, 2004). Of the trace elements in quartz from the Wusihe deposit, Li, K, Na generally increase from Q1 to Q2, and then decrease in Q3 veins through time. Reasonable linear correlations

between Al and these monovalent cations provide evidence for a component of coupled substitution in quartz where Al^{3+} and Li^{+}, K^{+}, or Na^{+} substitute for Si^{4+} (Fig. 7a-c). This suggests that the observed CL intensity variations may represent variations in the concentrations of Al and associated monovalent cations. Therefore, compensated substitution appears to be an important mechanism for the incorporation of Al into the quartz lattice in the Wusihe deposit.

Factors influencing Al concentrations in low-temperature hydrothermal quartz include temperature, growth rate, and aqueous Al concentration which is strongly influenced by Al solubility and pH in hydrothermal systems (Perny et al. 1992; Rusk et al. 2008; Götze and Möckel 2012). Sharp contrasts in Al concentration from zone to zone in single quartz grains from the Wusihe deposit, where no evidence for a temperature change exists, suggest that Al zoning in quartz does not result from temperature fluctuations. Crystal growth rate can also be ruled out, because in most samples, even where Al concentrations change by two orders of magnitude, no change in quartz morphology is observed (Rusk et al. 2008). Hence, Al concentrations in hydrothermal quartz from the Wusihe deposit likely reflect Al solubility and pH changes.

At Wusihe, Al concentrations in Q2 can reach 3049 ppm, suggesting quartz precipitated from Al-enriched acidic ore-forming fluids (Rusk et al. 2008). The

sharp contrast in Al concentrations from early Al-depleted quartz, to late dominant Al-rich quartz reflects acidification of neutral fluids led by sulfide precipitation (Rusk et al. 2008; Chen et al. 2011). This process is consistent with the reaction equation (1): $ZnCL_4^{2-}(aq) + H_2S(aq) = ZnS(s) + 2H^+ + 4Cl^-$ (Crerar et al. 1985; Talluri 2000; Leach et al. 2005; Hammerli et al. 2015). In Fig. 5j, k, the observed greyscale oscillatory zoning of Q2 may indicate that acid release was continuously buffered by dissolving carbonate wall rocks by the reaction equation (2): $CaCO_3(s) + 2H^+ = Ca^{2+} + H_2CO_3(aq)$. This reaction could facilitate solution collapse, providing space for further sulfide precipitation (Anderson and Macqueen 1982).

Furthermore, extensive SEM examination of authigenic K-feldspar (which preceded sphalerite growth, Fig. 5d-f) in ore samples did not reveal any evidence of alteration to sericite (muscovite) and kaolinite. Such alteration would be expected if the ore fluids had pH values < ~5-5.5 at 200°C (The homogenization temperature of fluid inclusions in sphalerite from the Wusihe deposit: 120-260°C; Fig. S1; Jones 1993; Rusk et al. 2008; Xiong et al. 2016). Therefore, this evidence suggests that the ore-forming fluids in the Wusihe deposit were weakly acidic.

Source of sulfur

Bulk $\delta^{34}S$ values measured in this study span an overall smaller range compared to those previously reported for the Wusihe deposit ($\delta^{34}S$ =

373 +7.1-+20.9‰; Lin 2005; Li 2007; Xiong et al. 2018; Zhu et al. 2018). On the
374 one hand, in agreement with previous research outcomes (Xiong et al. 2018;
375 Zhu et al. 2018), the ^{34}S-enriched sulfides in this study ($\delta^{34}S$ = +5.8-+14.3‰)
376 are indicative of products of marine evaporite minerals ($\delta^{34}S_{sulfate}$ =
377 +30.4‰-+35.3‰; Zhou et al. 2015, 2017; Kong et al. 2017; Yuan et al. 2017)
378 by thermochemical sulfate reduction (TSR). The majority of fluid inclusions
379 from the Wusihe deposit contain H_2S and CH_4 released by the thermal
380 degradation of organic matter (Xiong et al. 2016). Accordingly, subordinate
381 contributions of thermal degradation of organic matter (TDO) in sedimentary
382 rocks cannot be excluded (e.g. HR_aCH_2-S-H = $R_bCH2 + H_2S$; R_x represents a
383 large organic molecule) (Fig. 9a; Ohmoto 1972; Leventhal 1990). Conversely,
384 the presence of lower $\delta^{34}S$ values ($\delta^{34}S$<5‰) in this study suggests that the
385 sulfur in the Wusihe deposit may be derived from additional reservoirs (Fig. 9a).
386 Possibilities include i) H_2S from the basement granitic rocks or pyroclastic
387 rocks ($\delta^{34}S$=-5-+5‰; Ohmoto and Rye 1979), and ii) H_2S formed by bacterial
388 sulfate reduction (BSR) (Fig. 9a; Jorgensen et al. 1992).

389 The presence of ^{32}S-enriched sulfides may reflect fluids moving through
390 underlying Mesoproterozoic igneous basement or the Neoproterozoic Suxiong
391 Formation igneous rocks. However, there is almost no evidence for leaching
392 (e.g. field observations, C-O isotopes and REE patterns) of these igneous
393 rocks within the Wusihe district (e.g. Zheng 2012; Xiong et al. 2018; Zhu et al.

2018). Hence, igneous rocks are unlikely to contribute sulfur to the ore-forming fluid.

Open-system BSR can produce ^{32}S-enriched H_2S with a wide range of isotope fractionation (40-60‰) (Fig. 9a; Basuki et al. 2008). The biogenic H_2S mixed with H_2S produced by TSR may be the source of the lower $\delta^{34}S$ obtained in this study. The organic-enriched Qiongzhusi Fm. (black shales) could potentially serve as a reducing agent (e.g. $4R_x\text{-}CH_3 + 3SO_4^{2-} + H^+ = 4R_x\text{-}COOH + 4H_2O + 3H_2S$) (Leventhal 1990; Machel et al. 1995; Zhang et al. 2010; Wu 2013).

Variation of S isotopes

An increasing number of studies have shown that microscale variations in sulfur isotopic ratios obtained by in situ analysis of sulfur-bearing minerals can provide constraints on mineralizing process that cannot be resolved from bulk $\delta^{34}S$ values alone (Peevler et al. 2003; Xue et al. 2015). This is because traditional sampling techniques such as micro-drilling or mineral separation used to obtain sulfur isotopic compositions greatly exceed the observed scale of textual variation (μm) in pyrite and sphalerite (Xiong et al. 2018; Zhu et al. 2018).

Micro-scale analysis shows that the variation of $\delta^{34}S$ within a thin section is small (+0.5‰: +23.9-+24.4‰) in diagenetic samples, e.g. WSH-07, suggesting that diagenetic pyrite formed with no significant sulfur isotopic fractionation.

Considerable micro-scale variation exists among different grains in the lamellar pyrite (variation = +8.6‰: range = +18.0-+26.6‰) and even within single sphalerite grains in the massive ore (+12.3‰: +0.0-+12.3‰) (Fig. 10k, l). To better understand the large variation of $\delta^{34}S$ values at the single grain scale within the Wusihe deposit, the parameters affecting sulfur isotope signatures need to be evaluated.

Factors affecting the sulfur isotope signature of hydrothermal sulfide minerals include: *T*, *pH*, and fO_2 of the fluids as well as the $\delta^{34}S$ composition of the H_2S responsible for precipitating sulfide phases. As mentioned previously, fluid inclusion homogenization temperatures in the Wusihe deposit span a considerable range (120-260°C; Xiong et al. 2016), indicating appreciable temperature fluctuation during the course of sulfide precipitation. Temperature, however, is unlikely to have been a significant factor in producing the observed $\delta^{34}S$ variations, because sulfur isotopic fractionation between H_2S and ZnS/FeS_2 is insignificant and virtually independent of temperature (Fig. S2). Furthermore, there is almost no evidence that pyrite and barite co-exist in the Wusihe deposit, even though the Ba content of fluid inclusions obtained by LA-ICPMS are high spanning a range of 281-924 ppm (Li et al. unpublished data). Calculations presented by Ohmoto (1972) suggest that outside the pyrite-barite field, changes in pH and fO_2 would produce only very small variations in sulfide $\delta^{34}S$ (Fig. S3) Thus, the observed variations in $\delta^{34}S$

appear to have been controlled predominantly by the $\delta^{34}S$ composition of H_2S during sulfide deposition.

The $\delta^{34}S$ of stage-I pyrite is close to that of diagenetic pyrite and higher than that of stages-II and -III grains, suggesting that stage-I pyrite formed through nearly close-system BSR with no significant fractionation (Fig. 9a). Micro-scale variations in sulfur isotopes show an increasing trend of $\delta^{34}S$ values from core to rim in stage-II and -III pyrite and sphalerite (Figs. 9c and 10k, l), suggesting more ^{32}S-riched H_2S produced by BSR was incorporated during early formation. BSR can only take place at temperatures of <~110°C (Jorgensen et al. 1992). However, prior to the arrival of hydrothermal fluids, the ambient temperatures during the transition from the late Ediacaran to early Cambrian, were likely <110°C (Xue et al. 2015). Accordingly, the formation of a local H_2S reservoir prior to the arrival of ore-forming fluids cannot be ruled out. As the temperature of the mineralizing fluids were episodically raised to more than 120°C (inferred from fluid inclusion data; e.g. Xiong et al. 2016), the site of mineralization would inhibit BSR and promote TSR. Hence, the mixing of different proportions of H_2S reduced by BSR and TSR are capable of producing the observed range of S isotope values.

Source of metals

As shown on Fig. 11a, our new homogeneous Pb isotope data plot above the upper crust evolution line, suggesting a homogeneous or well-mixed metal

source originating in the upper crust. Secondly, the coarse-grained massive galena aggregates have distinct Pb isotopic compositions relative to the fine-grained brecciated and banded sulfide ores (Fig. 11b, c). Considering that the U and Th contents of galena are negligible, Pb isotopic ratios of galena formed at different paragenetic stages likely reflect the composition of hydrothermal fluids (Zhou et al. 2018b). The data suggest that the two stages of ore-forming fluids had distinct Pb isotopic compositions (Fig. 11b，c) . Highly radiogenic Pb from wall rock sequences (e.g. late Ediacaran sedimentary rocks) are inferred to have provided a greater contribution during stage-II mineralization than stage-III.

Fig. 11d shows the in situ Pb isotopic results from this study, along with previous in situ data from the Upper Yangtze Pb-Zn metallogenic province for comparison (Bao et al. 2017; Tan et al. 2017; Zhou et al. 2018a, b, c; Luo et al. 2019). The data show that in situ Pb isotopic compositions vary between deposits, and that variations correlate directly with the age of the host rock. Galena in situ Pb isotope ratios become increasingly radiogenic from Pb-Zn deposits hosted in Cambrian strata (e.g. the Nayongzhi and Maliping deposits), to those Pb-Zn deposits hosted in Upper Ediacaran strata (e.g. the Wusihe and Yinchanggou deposits), and further still for Pb-Zn deposits in Carboniferous-Permian strata in this province (e.g. the Maozhachang, Liangyan and Huize deposits). This pattern might have resulted from: i) the

478 variable accumulation of radiogenic Pb due to variations in parental U and Th
479 concentrations, ii) heterogeneity of the Pb isotopic signature of basement
480 rocks, iii) the evolution (e.g. migration, precipitation) of a single source material
481 (e.g. basement source rocks), or iv) the interaction of separate and isotopically
482 distinct Pb sources (e.g. Moyers 2015; Potra et al. 2018). The first scenario
483 can be excluded because trace element LA-ICPMS data show that there is no
484 significant difference in the U and Th contents of galena among these deposits
485 (Ye Lin et al. 2011 and unpublished data). The slopes may imply that the
486 Maliping, Wusihe and Yinchanggou deposits are separate from the Nayongzhi,
487 Huize, Liangyan, Maozhachang and Fule deposits, the two groups defining
488 separate age clusters, supported by radiogenic dating results (dashed lines in
489 Fig. 11d; Wu 2013; Zhang et al. 2014; Xiong et al. 2018; Zhou et al. 2013b,
490 2015, 2018a and references therein). This pattern could potentially result from
491 the evolution of a single source material. However, the fluid driving mechanism
492 in this province during mineralization was considered to be local non-aquifer
493 tectonically-driven fluid expulsion from orogenic belts (Han et al. 2007), which
494 is different to that of the Mississippi Valley, or eastern Australia where
495 topographically-driven gravitational fluid flow occurred via long-distance /
496 large-scale migration along sandstone aquifers (Appold and Garven 1999;
497 Huston et al. 2017). Our new Pb isotope data plot on the upper margin of the
498 broad field of basement rocks, whilst Devonian to Permian carbonate rocks

This is a preprint, the final version is subject to change, of the American Mineralogist (MSA)
Cite as Authors (Year) Title. American Mineralogist, in press.
DOI: https://doi.org/10.2138/am-2020-7021

499 extend to significantly more radiogenic compositions (Fig. 11a, d). Hence, in
500 addition Pb isotope variations related to the age of the host rocks, part of the
501 observed scatter may reflect the isotopic heterogeneity of the basement.
502 However, a local mixture of less radiogenic Pb (low $^{207}Pb/^{204}Pb$) from
503 basement rocks and more radiogenic Pb (high $^{207}Pb/^{204}Pb$) originating from
504 carbonate wall rocks cannot be ruled out.
505
506 **IMPLICATIONS**
507 **Ore-forming environments**
508 It is generally accepted that most major low-temperature hydrothermal
509 deposits formed during large-scale contractional events during nearby
510 orogenic activity (e.g. Hu et al. 2017; Leach et al. 2010). These deposits
511 include hydrothermal Hg, Carlin-type Au deposits (e.g. Hu et al. 2017) and the
512 MVT Pb-Zn deposits featured in this study (Fig. 1; e.g. Zhang 2008; Duan et al.
513 2014; Xiong et al. 2018; Zhou et al. 2018b). When continental margins in
514 mountain belts are buried beneath thrust sheets, hydrothermal fluids expelled
515 from marginal sediments migrate into the foreland basin and continental
516 interior. These fluids are involved in faulting, migration of hydrocarbons and
517 metals, metamorphism, paleomagnetism, and final ore concentration (Oliver
518 1986; Appold and Nunn 2005). This environment is consistent with that along
519 the margins of the Yangtze Block (Fig. 1b; e.g. Li et al. 2002; Hu et al. 2017),

where numerous previous studies suggest that the formation of low-temperature hydrothermal deposits, occurred in various basin-mountain systems (Fig. 1b), coincided with collision compression and post-collisional extension related to the late Caledonian and the late Indochina orogenies (e.g. Xiong et al. 2018; Zhou et al. 2018b).

In addition to tectonic setting, wall rock sequences appear to be more important in concentrating ores than previously thought. Pb-Zn deposits surrounding the Yangtze Block are primarily hosted in carbonate rocks of the late Ediacaran-early Cambrian and the early Devonian-early Permian (Huang 2004; Zhou et al. 2018b). Among these two sequences, the late Ediacaran Dengying Formation is the dominant host of Pb-Zn orebodies. This is likely because: 1) the Dengying Formation comprises thickly-bedded siliceous, evaporitic dolostones with high porosity, interlayered with numerous H_2S-bearing hydrocarbon reservoirs (Shao and Li 1996; Wu et al. 2013; Lin 2014); 2) extensive pre-existing karst cavities and interlayered faulted zones present in this sequence provided the necessary space for the formation of high-grade ores (Lin 2014); and 3) the immediately overlying organic-rich marine black shales of the early Cambrian Qiongzhusi Formation are thermally mature and contain up to 22.3% total organic carbon (TOC), most of which yields type-I kerogen (Zou et al. 2010). The shales provided an important source of oil and hydrocarbons, supported by the large volume of solid

541 bitumen degraded via pyrolysis which characterizes the Wusihe district (e.g.
542 Zhang et al. 2010; Zheng 2012; Luo et al. 2019). Hence, this constitutes an
543 aquitard plus a key geochemical reduction barrier for migrating fluids (e.g.).
544 This arrangement is in agreement with the occurrence of the ~50 km long
545 ore-hosting belt located in the Wusihe district.

546 **The precipitation mechanism for sulfide minerals**

547 There are three identified precipitation mechanisms for sulfides in MVT
548 deposits, including: 1) the reduced sulfur mechanism; 2) the local sulfate
549 reduction mechanism; and 3) the metal and reduced sulfur-mixing mechanism
550 (Leach et al. 2005 and references therein). At Wusihe, the reduced sulfur
551 mechanism can be excluded because the pH of the predicted mineralizing
552 solution was likely too high (>~5.5) (as suggested by the presence of
553 authigenic K-feldspar), and hence the reduced sulfur and metals were
554 probably not delivered via a single fluid (Sverjensky 1984; Emsbo 2000). The
555 presence of extensive fine-grained and colloform textured sphalerite of stage-I
556 indicate a fluid-mixing mechanism in the Wusihe deposit (Fig. 3; Corbella et al.
557 2004; Zhang et al. 2009). The local sulfate reduction mechanism could
558 dominantly lead to stage-II and -III sulfide precipitation, with typically large,
559 well-formed sulfides reflecting slow H_2S generation, and organic matter
560 derived from ore-hosting wall rocks (Anderson et al. 2015; Xiong et al. 2016).

This is a preprint, the final version is subject to change, of the American Mineralogist (MSA)
Cite as Authors (Year) Title. American Mineralogist, in press.
DOI: https://doi.org/10.2138/am-2020-7021

Evolution of the hydrothermal system

Through an integrated approach, this paper proposes a new working model to explain the Pb-Zn mineralization in the Wusihe district (Fig. 12a). Within the western margin of the Yangtze Block, hot and weakly acidic brines (e.g. $H_2S_{(aq)} + O_{2\ (aq)} = SO_4^{2-} + 2H^+$; Corbella and Ayoma 2003), driven by the late Caledonian orogeny (411 ± 10Ma; sphalerite Rb-Sr; Xiong et al. 2018), extracted metals primarily from the basement rocks, potentially followed by a limited contribution from local carbonate wall rocks (as suggested by Pb isotopes, this study), to form metal-bearing chloride in ore-forming fluids. These fluids migrated along the Ganluo-Xiaojiang fault zone into unconformities and interlayered fault zones associated with the Wanlicun syncline in the Wusihe district (e.g. Han et al. 2007). This is supported by the presence of authigenic K-feldspar in the Wusihe deposit which required the flux of multiple pore volumes of fluid through the rocks, reflecting fluid migration events during orogenic activity. The fluids interacted with the ^{34}S-enriched pre-existing H_2S generated in situ, largely through close-system BSR (<~110°C) at the deposition site during the first stage of mineralization (stage-I), forming the lower group of the deposition site. Due to variable mineral compositions, porosity and permeability of the wall rocks, these ore fluids selectively replaced some of the parallel organic-bearing fissure layers in the wall rocks, forming lamellar ores with clear boundaries between sulfide

582 layers.

583 Meanwhile, a ^{32}S-enriched H_2S reservoir generated by open-system BSR
584 formed before the arrival of the high-T ore-forming fluid within the upper group
585 of the deposition site (stages-II and -III). The organic-rich Qiongzhusi
586 Formation may have served as a reducing agent. When the fluids ascended,
587 the mineralization system yielded ^{34}S-enriched H_2S because the high
588 temperature of the fluids inhibited BSR and promoted TSR. Proximal to faults,
589 fluids containing Pb-Zn chloride complexes rapidly mixed with the H_2S
590 reservoir and cooled to form hydrothermal collapse breccia fragments,
591 fine-grained stock-work and brecciated ores. The relatively Pb-enriched fluids
592 formed massive ore. The sulfide precipitation processes outlined above
593 correspond to an acid-producing chemical reaction (as suggested by Al
594 concentrations). This reaction enhanced the acidity of fluids, resulting in further
595 dissolution of surrounding wall rock carbonates, thereby providing additional
596 space for further sulfide precipitation during ore-forming processes.

597

598 **ACKNOWLEDGEMENTS**

599 This research was financially supported by National Natural Science
600 Foundation of China (41872095 and 41430315), the National Key R&D
601 Program of China (2017YFC0602502), and the Research Start-up Project for
602 Introduced Talent of Yunnan University (YJRC4201804) and the Cultivation

603 Project for Excellent Youth of National Natural Science Foundation of Yunnan
604 University (2018YDJQ009) to J.-X. Zhou. We thank Dr. Wei Zhou, Gang Xia
605 (The University of Queensland, Australia), Dr. En-Tao Liu (China University of
606 Geosciences, Wuhan, China), Prof. Tai-Yi Luo and Dr. Jun Chen, Zhen-li Li
607 (Institute of Geochemistry, Chinese Academy of Sciences, China) for fruitful
608 discussions. Comments and suggestions from Prof. Fang-Zhen Teng
609 (Associate Editor), Prof. Martin Appold, David Huston and the anonymous
610 reviewer greatly improved the quality of the paper.

REFERENCES CITED

Anderson, G., Macqueen, R. (1982) Ore deposit models-6. Mississippi Valley-type lead-zinc deposits. Geoscience Canada 9 (2).

Anderson, G. (2015) Kerogen as a source of sulfur in MVT deposits. Economic Geology, 110, 837-840.

Appold, M., Nunn, J.A. (2005) Hydrology of the Western Arkoma basin and Ozark platform during the Ouachita orogeny: Implications for Mississippi Valley-type ore formation in the Tri-State Zn-Pb district. 5, 308-325.

Appold, M., Garven, G. (1999) The hydrology of ore formation in the Southeast Missouri district: Numerical models of topography-driven fluid flow during the Ouachita Orogeny. Economic Geology and the Bulletin of the Society of Economic Geologists, 94, 913-935.

Bao, Z., Li, Q., and Wang, C.Y. (2017) Metal source of giant Huize Zn-Pb deposit in SW China: New constraints from in situ Pb isotopic compositions of galena. Ore Geology Reviews, 91, 824-836.

Basuki, N.I., Taylor, B.E., Spooner, E.T.C. (2008) Sulfur Isotope Evidence for Thermochemical Reduction of Dissolved Sulfate in Mississippi Valley-Type Zinc-Lead Mineralization, Bongara Area, Northern Peru. Economic Geology, 103, 783-799.

Beck, W.R. (1949) Crystallographic inversions of the aluminum

632 orthophosphate polymorphs and their relation to those of silica. Journal
633 of the American Ceramic Society, 32, 147-151.
634 Chen, X.D., Chen ZY, Cheng YB, Ye HS, Wang H (2011) Distribution and
635 Application of Trace Elements in Hydrothermal Quartz: Understanding
636 and prospecting. Geological Review, 57, 707-717. (in Chinese with
637 English abstract)
638 Chu, Y., Lin, W., Faure, M., Wang, Q.C., Ji, W.B. (2012) Phanerozoic
639 tectonothermal events of the Xuefengshan Belt, central South China:
640 Implications from U-Pb age and Lu-Hf determinations of granites. Lithos,
641 150, 243-255.
642 Corbella, M., Ayora, C. (2003) Role of fluid mixing in deep dissolution of
643 carbonates. Geologica Acta, 1, 305.
644 Corbella, M., Ayora, C., Cardellach, E. (2004) Hydrothermal mixing, carbonate
645 dissolution and sulfide precipitation in Mississippi Valley-type deposits.
646 Mineralium Deposita, 39, 344-357.
647 Crerar, D., Wood, S., Brantley, S., Bocarsly, A. (1985) Chemical controls on
648 solubility of ore-forming minerals in hydrothermal solutions. The
649 Canadian Mineralogist, 23, 333-352.
650 Duan, Q.F. (2014) The research of metallogenic regularity of stritabound
651 zinc-lead deposits from Sinian-Cambrian in western Hunan and western
652 Hubei. (in Chinese with English abstract)

653 Duan, Q.F., Cao, L., Zeng, J.K., Zhou, Y., Tang, C.Y., Li, K. (2014) Rb-Sr
654 Dating of Sphalerites from Shizishan Pb-Zn Deposit in Huayuan Ore
655 Concentration Area,Western Hunan,and Its Geological Significance.
656 Earth Science, 39, 977-986 and 999.
657 Durham, K.C. (1966) Role of juvenile solutions, connate waters and evaporitic
658 brines in the genesis of lead zinc-fluorine-barium deposits: Transactions,
659 Institution of Mining and Metallurgy, sec. B, v. 75, p. B226-229.
660 Emsbo, P. (2000) Gold in sedex deposits. Reviews in Economic Geology, v. 13,
661 p. 427–438.
662 Gibbins, W.A. (1983) Mississippi Valley type lead-zinc districts of northern
663 Canada, In P roceedings, International Conference on Mississippi
664 Valley Type Lead-Zinc Deposits, University of Missouri-Rolla, pp.
665 403-414.
666 Gotze, J., Plotze, M., Habermann, D. (2001) Origin, spectral characteristics
667 and practical applications of the cathodolumimescence (CL) of quartz -
668 a review. Mineralogy and Petrology, 71, 225-250.
669 Götze, J., Plötze, M., Graupner, T., Hallbauer, D.K., Bray, C.J. (2004) Trace
670 element incorporation into quartz: A combined study by ICP-MS,
671 electron spin resonance, cathodoluminescence, capillary ion analysis,
672 and gas chromatography. Geochimica et Cosmochimica Acta, 68,
673 3741-3759.

674 Götze, J., Möckel, R. (2012) Quartz: Deposits, mineralogy and analytics.
675 Springer Science & Business Media.
676 Guilbert, John M. and Charles F. Park. (1986) The Geology of Ore Deposits, W.
677 H. Freeman, pp 889–907.
678 Hammerli, J., Spandler, C., Oliver, N.H., Sossi, P., Dipple, G.M. (2015) Zn and
679 Pb mobility during metamorphism of sedimentary rocks and potential
680 implications for some base metal deposits. Mineralium Deposita, 50,
681 657-664.
682 Han, R.S., Liu, C.Q., Huang, Z.L., Chen, J., Ma, D.Y., Lei, L., Ma, G.S. (2007)
683 Geological features and origin of the Huize carbonate-hosted
684 Zn-Pb-(Ag) District, Yunnan, South China. Ore Geology Reviews, 31,
685 360-383.
686 Hou, Z.Q., Wang, S.X., Du, A.D., Qu, X.M., Sun, W.D. (2003) Re-Os dating of
687 sulfides from the volcanogenic massive sulfide deposit at Gacun,
688 southwestem China. Resource Geology, 53, 305-310.
689 Hu, R.Z., Fu, S.L., Huang, Y., Zhou, M.F., Fu, S.H., Zhao, C.H., Wang, Y.J., Bi,
690 X.W., Xiao, J.F. (2017) The giant South China Mesozoic
691 low-temperature metallogenic domain: Reviews and a new geodynamic
692 model. Journal of Asian Earth Sciences, 137, 9-34.
693 Huang, Z.L., Chen, J., Han, R.S., Li, W.B., Liu, C.Q., Zhang, Z.L., Ma, D.Y.,
694 Gao, D.R., Yang, H.L. (2004) Geochemistry and Ore-formation of the

695 Huize Giant Lead-zinc Deposit, Yunnan, Province, China: Discussion
696 on the Relationship Between Emeishan Flood Basalts and Lead-zinc
697 Mineralization, pp.1–154. Geological Publishing House, Beijing (in
698 Chinese).
699 Huang, J.L., Zou, C.N., Li, J.Z., Dong, D.Z., Wang, S., Wang, S.Q., Cheng,
700 K.M. (2012) Shale gas generation and potential of the Lower Cambrian
701 Qiongzhusi Formation in the Southern Sichuan Basin, China. Petroleum
702 Exploration and Development 39, 75-81.
703 Huston, D., Champion, D., Morrison, G., Maas, R., Thome, J.P., Carr, G.,
704 Beams, S., Bottrill, R., Chang, Z., Dhnaram, C., Downes, P., Forster, D.,
705 Gemmell, B., Lisitsin, V., McNeil, A., and Vicary, M. (2017) Spatial
706 variations in lead isotopes, Tasman Element, eastern Australia.
707 Huston, D.L., Stevens, B., Southgate, P.N., Muhling, P., Wyborn, L. (2006)
708 Australian Zn-Pb-Ag ore-forming systems: a review and analysis.
709 Economic Geology, 101, 1117-1157.
710 Huttenlocher, H.F. (1935) Crystal structure of aluminium orthophosphate
711 AlPO4. Zeitschrift Fur Kristallographie, 90, 508-516.
712 Jiang, Y.H., Jin, G.D., Liao, S.Y., Zhou, Q., Zhao, P. (2010) Geochemical and
713 Sr–Nd–Hf isotopic constraints on the origin of Late Triassic granitoids
714 from the Qinling orogen, central China: Implications for a continental arc
715 to continent–continent collision. Lithos, 117, 183-197.

716 Jones, H.D. (1993) Geochemical and sulfur isotopic investigations into the
717 origins of Mississippi Valley-type mineralization in the southern
718 Appalachians and nearby areas (Doctoral dissertation).
719 Jorgensen, B.B., Isaksen, M.F., Jannasch, H.W. (1992) Bacterial sulfate
720 reduction above 100°C in deep-sea hydrothermal vent sediments.
721 Science, 258, 1756-1757.
722 Kajiwara, Y., Krouse, H. (1971) Sulfur isotope partitioning in metallic sulfide
723 systems. Canadian Journal of Earth Sciences, 8, 1397-1408.
724 Kong, Z.G., Wu, Y., Liang, T., Zhang, F., Meng, X.Y., Lu, L. (2017) Sources of
725 ore-forming material for Pb-Zn deposits in the Sichuan-Yunnan-
726 Guizhou triangle area: Multiple constraints from C-H-O-S-Pb-Sr
727 isotopic compositions. Geological Journal, 53, 159-177.
728 Kucha, H. (2010) Microbial Sphalerite Formation in Carbonate-Hosted Zn-Pb
729 Ores, Bleiberg, Austria: Micro- to Nanotextural and Sulfur Isotope
730 Evidence. Economic Geology, 105, 1005-1023.
731 Lan, T.G., Hu, R.Z., Bi, X.W., Mao, G.J., Wen, B.J., Liu, L., Chen, Y.H. (2018)
732 Metasomatized asthenospheric mantle contributing to the generation of
733 Cu-Mo deposits within an intracontinental setting: a case study of the~
734 128 Ma Wangjiazhuang Cu-Mo deposit, eastern North China Craton.
735 Journal of Asian Earth Sciences, 160, 460-489.
736 Leach, D.L., Sangster, D.F., Kelley, K.D., Large, Ross. R., Garven, G., Allen,

C.R. (2005) Sediment-hosted Pb-Zn Deposits: a global perspective. Economic Geology, 100, 561-608.

Leach, D.L., Bradley, D.C., Huston, D., Pisarevsky, S.A., Taylor, R.D., Gardoll, S.J. (2010) Sediment-hosted lead-zinc deposits in Earth history. Economic Geology, 105, 593-625.

Leventhal, J.S., 1990. Organic matter and thermochemical sulfate reduction in the Viburnum Trend, Southeast Missouri. Economic Geology, 85, 622-632.

Li, X.H., Li, Z.X., Li, W.X., Wang, Y. (2006) Initiation of the Indosinian Orogeny in South China: evidence for a Permian magmatic arc on Hainan Island. The Journal of geology, 114, 341-353.

Li, Y., He, D., Li, D., Lu, R., Fan, C., Sun, Y., Huang, H. (2018) Sedimentary provenance constraints on the Jurassic to Cretaceous paleogeography of Sichuan Basin, SW China. Gondwana Research, 60, 15-33.

Li, T.Z. (2007) The genesis and metallogenic model oflead-zinc deposits in the middle part of Dadu River Valley. MSc thesis, Chengdu Institute of Technology, Chengdu, China, pp. 1-55. (in Chinese with English abstract)

Lin, F.C. (2005) Geological and geochemical characteristics and genesis ofsupper-large-scale Sedex-type stratiform lead-zinc deposits in the Dadu River Valley on the western margin of the Yangtze Craton. Acta

758 Geologica Sinica, 79, 540-556. (in Chinese with English abstract)
759 Liu, H.C., Lin, W.D. (1999) Study on the Pb–Zn–Ag ore deposits in northeast
760 Yunnan, Yunnan, China. Yunnan University Press, Kunming, pp. 1-468
761 (in Chinese)
762 Liu, Y.S., Hu, Z.C., Gao, S., Günther, D., Xu, J., Gao, C.G., Chen, H.H. (2008)
763 In situ analysis of major and trace elements of anhydrous minerals by
764 LA-ICP-MS without applying an internal standard. Chemical Geology,
765 257, 34-43.
766 Lu, S., Li, H., Chen, Z., Hao, G., Zhou, H., Guo, J., Niu, G., Xiang, Z. (2003)
767 Meso-Neoproterozoic geological evolution in the Qinling orogeny and
768 its response to the supercontinental events of Rodinia. Geological
769 Publish House, Beijing: 1-194.
770 Li, J.W., Vasconcelos, P., Zhou, M.F., Deng, X.D., Cohen, B., Bi, S.J., Zhao,
771 X.F., Selby, D. (2014) Longevity of magmatic–hydrothermal systems in
772 the Daye Cu–Fe–Au District, eastern China with implications for mineral
773 exploration. Ore Geology Reviews, 57, 375-392.
774 Lin, X.X. (2014) Study on dolomite and metallogenic regularity of lead-zinc
775 deposits within the Sinian Dengying Formation in Hanyuan region,
776 Sichuan Province, China. (In Chinese with English abstract)
777 Luo, K., Zhou, J.X., Huang, Z.L., Wang, X.C., Wilde, S.A., Zhou, W., and Tian,
778 L. (2019) New insights into the origin of early Cambrian

779 carbonate-hosted Pb-Zn deposits in South China: A case study of the
780 Maliping Pb-Zn deposit. Gondwana Research, 70, 88-103.
781 Machel, H.G., Krouse, H.R., Sassen, R., 1995. Products and distinguishing
782 criteria of bacterial and thermochemical sulfate reduction. Appllied
783 Geochemistry, 10, 373–389.
784 Mackey, J.H. (1963) EPR Study of Impurity-Related Color Centers in
785 Germanium-Doped Quartz. Journal of Chemical Physics, 39, 74-83.
786 Maschmeyer, D., Lehmann, G. (1983) A trapped-hole center causing rose
787 coloration of natural quartz. Zeitschrift Fur Kristallographie, 163,
788 181-196.
789 Mi, M., Chen, Y.J., Yang, Y.F., Wang, P., Li, F.L., Wan, S.Q., Xu, Y.L. (2015)
790 Geochronology and geochemistry of the giant Qian'echong Mo deposit,
791 Dabie Shan, eastern China: Implications for ore genesis and tectonic
792 setting. Gondwana Research, 27, 1217-1235.
793 Moyers, A. (2015) Source Constraints of Ore Metals In Mississippi Valley-Type
794 Deposits in Central and Eastern Tennessee Using Pb Isotopes.
795 Dissertations & Theses - Gradworks.
796 Ohmoto, H. (1972) Systematics of Sulfur and Carbon Isotopes in Hydrothermal
797 Ore Deposits. Economic Geology, 67, 551-578.
798 Ohmoto, H., Rye, R. (1979) Isotopes of sulfur and carbon. Geochemistry of
799 hydrothermal ore deposits. 509-567.

800 Ohmoto, H. (1986) Stable isotope geochemistry of ore-deposits. Reviews in
801 Mineralogy, 16, 491-559.
802 Oliver, J. (1986). Fluids expelled tectonically from orogenic belts: Their role in
803 hydrocarbon migration and other geologic phenomena. Geology, 14,
804 99-102.
805 Paradis, S., Hannigan, P., Dewing, K. (2007) Mississipi valley-type lead-zinc
806 deposits (MVT). Mineral deposits of Canada, Geological Survey of
807 Canada. 1-15.
808 Peevler, J., Fayek, M., Misra, K.C., Riciputi, L.R. (2003) Sulfur isotope
809 microanalysis of sphalerite by SIMS: constraints on the genesis of
810 Mississippi valley-type mineralization, from the Mascot-Jefferson City
811 district, East Tennessee. Journal of Geochemical Exploration, 80,
812 277-296.
813 Perny, B., Eberhardt, P., Ramseyer, K., Mullis, J., Pankrath, R. (1992)
814 Microdistribution of Al, Li, and Na in α quartz: possible causes and
815 correlation with short-lived cathodoluminescence. Am Mineral.
816 American Mineralogist, 77, 534-544.
817 Potra, A., Garmon, W.T., Samuelsen, J.R., Wulff, A., Pollock, E.D. (2018) Lead
818 isotope trends and metal sources in the Mississippi Valley-type districts
819 from the mid-continent United States. Journal of Geochemical
820 Exploration, 192, 174-186.

821 Roger, F., Malavieille, J., Leloup, P.H., Calassou, S., Xu, Z. (2004) Timing of
822 granite emplacement and cooling in the Songpan–Garzê Fold Belt
823 (eastern Tibetan Plateau) with tectonic implications. Journal of Asian
824 Earth Sciences, 22, 465-481.
825 Rusk, B.G., Lowers, H.A., Reed, M.H. (2008) Trace elements in hydrothermal
826 quartz: Relationships to cathodoluminescent textures and insights into
827 vein formation. Geology, 36, 547-550.
828 Rye, R., Czamanske, G. (1969) Experimental determination of
829 sphalerite-galena sulfur isotope fractionation and application to ores at
830 Providencia, Mexico Geological Society of America Abstract, pp.
831 195-196.
832 Sakai, H. (1969) Sulfur isotopes and the Pine Point lead-zinc mineralization.
833 Economic Geology, 64, 718-730.
834 Shao, S.C., Li, C.Y. (1996). Metallogenetic rules of the strata-bound Pb-Zn
835 deposit in Dengying Formation of the west margin of Yangtze massif
836 and its possibility of ore-forming super-large ore deposit. Yunnan
837 Geology. (In Chinese with English abstract)
838 Shu, L.S. (2006) Predevonian tectonic evolution of south China: from
839 Cathaysian Block to Caledonian period folded orogenic belt. Geological
840 Journal of China Universities, 12, 418-431.
841 Song, Y.C., Yang, T.N., Zhang, H.R., Liu, Y.C., Hao, H.D., Li, Z. (2015) The

842 Chaqupacha Mississippi Valley-type Pb–Zn deposit, central Tibet: Ore
843 formation in a fold and thrust belt of the India–Asia continental collision
844 zone. Ore Geology Reviews, 70, 533-545.
845 Sverjensky, D.A. (1981) The origin of a Mississippi Valley-type deposit in the
846 Viburnum Trend, Southeast Missouri. Economic Geology, 76,
847 1848-1872.
848 Sverjensky, D.A. (1984) Oil field brines as ore-forming solutions. Economic
849 Geology, 79, 23-37.
850 Talluri. (2000) Fluid Chemistry and Depositional Mechanism of the Epigenetic,
851 Discordant Ores of the Proterozoic, Carbonate-Hosted, Zawarmala
852 Pb-Zn Deposit, Udaipur District, India. Economic Geology, 95,
853 1505-1525.
854 Tan, S.C., Zhou, J.X., Li, B., Zhao, J.X. (2017) In situ Pb and bulk Sr isotope
855 analysis of the Yinchanggou Pb-Zn deposit in Sichuan Province (SW
856 China): Constraints on the origin and evolution of hydrothermal fluids.
857 Ore Geology Reviews, 91, 432-443.
858 Wallis, S., Tsujimori, T., Aoya, M., Kawakami, T., Terada, K., Suzuki, K., Hyodo,
859 H. (2003) Cenozoic and Mesozoic metamorphism in the Longmenshan
860 orogen: Implications for geodynamic models of eastern Tibet. Geology,
861 31, 745-748.
862 Wang, C.M., Deng, J., Carranza, E.J.M., Lai, X.R. (2014) Nature, diversity and

temporal–spatial distributions of sediment-hosted Pb—Zn deposits in China. Ore Geology Reviews, 56, 327-351.

Wang, L.J., Yu, J.H., Griffin, W.L., O'Reilly, S.Y. (2012) Early crustal evolution in the western Yangtze Block: Evidence from U–Pb and Lu–Hf isotopes on detrital zircons from sedimentary rocks. Precambrian Research 222-223, 368-385.

Wang, X., Xue, C., Li, Z., Li, Q., Yang, R. (2008) Geological and geochemical characteristics of Mayuan Pb-Zn ore deposit on northern margin of Yangtze landmass. Mineral Deposits - Bejing, 27, 37.

Wang, Y.J., Zhang, F.F., Fan, W.M., Zhang, G.W., Chen, S.Y., Cawood, P.A., Zhang, A.M. (2010) Tectonic setting of the South China Block in the early Paleozoic: Resolving intracontinental and ocean closure models from detrital zircon U-Pb geochronology. Tectonics, 29.

Wilkinson, J. (2013) Sediment-Hosted Zinc-Lead Mineralization: Processes and Perspectives. Processes and Perspectives, Treatise on Geochemistry, Elsevier, H Holland, K Turekian (ed), Amsterdam, Netherlands, pp. 219-249. Doi:10.1016/B978-0-08-095975-7.01109-8.

Wilkinson, J.J., Eyre, S.L., Boyce, A.J. (2005) Ore-forming processes in Irish-type carbonate-hosted Zn-Pb deposits: Evidence from mineralogy, chemistry, and isotopic composition of sulfides at the Lisheen mine. Economic Geology, 100, 63-86.

884 Wu, T., Xiao, L., Wilde, S.A., Ma, C.Q., Zhou, J.X. (2017) A mixed source for
885 the Late Triassic Garzê-Daocheng granitic belt and its implications for
886 the tectonic evolution of the Yidun arc belt, eastern Tibetan Plateau.
887 Lithos, 288, 214-230.
888 Wu, T., Zhou, J.X., Wang, X.C., Li, W.X., Wilde, S.A., Sun, H.R., Wang, J.S., Li,
889 Z. (2018). Identification of ca. 850 Ma high-temperature strongly
890 peraluminous granitoids in southeastern Guizhou Province, South
891 China: A result of early extension along the southern margin of the
892 Yangtze Block. Precambrian Research, 308, 18-34.
893 Wu, Y. (2013).The age and ore-forming process of MVT deposits in the
894 boundary area of Sichuan -Yunnan-Guizhou provinces, Southwest
895 China. A dissertation submitted to China University of Geosciences.
896 Beijing (In Chinese with English abstract)
897 Wu, Y., Zhang, C.Q., Mao, J.W., Ouyang, H.G., Sun, J. (2013) The genetic
898 relationship between hydrocarbon systems and Mississippi Valley-type
899 Zn-Pb deposits along the SW margin of Sichuan Basin, China.
900 International Geology Review, 55, 941-957.
901 Xiong, S.F., Yao, S.Z., Gong, Y.J., Tang, M.T., Zeng, G.P., Wang, W. (2016)
902 Ore-forming fluid and thermochemical sulfate reduction in the Wusihe
903 lead-zinc deposit, Sichuan Province, China. Earth Science 41, 105–120.
904 (in Chinese with English abstract)

905 Xiong, S.F., Gong, Y.J., Jiang, S.Y., Zhang, X.J., Li, Q., Zeng, G.P. (2018) Ore
906 genesis of the Wusihe carbonate-hosted Zn-Pb deposit in the Dadu
907 River Valley district, Yangtze Block, SW China: evidence from ore
908 geology, S-Pb isotopes, and sphalerite Rb-Sr dating. Mineralium
909 Deposita, 1-13.
910 Xue, C., Chi, G., Fayek, M. (2015) Micro-textures and in situ sulfur isotopic
911 analysis of spheroidal and zonal sulfides in the giant Jinding Zn–Pb
912 deposit, Yunnan, China: Implications for biogenic processes. Journal of
913 Asian Earth Sciences, 103, 288-304.
914 Ye, L., Cook, N. J., Ciobanu, C. L., Yuping, L., Qian, Z., Tiegeng, L. (2011)
915 Trace and minor elements in sphalerite from base metal deposits in
916 south china: a LA-ICPMS study. Ore Geology Reviews, 39, 188-217.
917 Yuan, S.D., Ellis, G.S., Chou, I.M., Burruss, R.C. (2017) Experimental
918 investigation on thermochemical sulfate reduction in the presence of
919 1-pentanethiol at 200 and 250° C: Implications for in situ TSR
920 processes occurring in some MVT deposits. Ore Geology Reviews, 91,
921 57-65.
922 Zartman, R.E., Doe, B.R. (1981) Plumbotectonics - the model. Tectonophysics,
923 75, 135-162.
924 Zhang, C.Q. (2008) The genetic model of Mississippi Valley-type deposits in
925 the boundary area of Sichuan, Yunnan and Guizhou Province, China.

926 PhD thesis, Chinese Academy of Geological Sciences, Beijing (in
927 Chinese with English abstract).
928 Zhang, C.Q., Li, X.B., Yu, J.J., Mao, J.W., Chen, F.K., Li, H.M. (2008) Rb–Sr
929 dating of single sphalerites from the Daliangzi Pb–Zn deposit, Sichuan,
930 and its geological significances. Geological Review, 54, 145-151 (in
931 Chinese with English abstract).
932 Zhang, C.Q., Yu, J.J., Mao, J.W., Yu, H., Li, H.M. (2010) Research on the
933 Biomarker from Chipu Pb-Zn Deposit, Sichuan. Acta Sedimentologica
934 Sinica, 28, 832-844. (In Chinese with English abstract).
935 Zhang, C.Q., Wu, Y., Wang, D.H., Chen, Y.C. (2014) Brief introducition on
936 metallogeny of Pb-Zn deposits in China. Acta Geologica Sinica, 88,
937 2252-2268. (In Chinese with English abstract).
938 Zhang, C.Q., Yu, J.J., Mao, J.W., Rui, Z.Y. (2009) Advances in the study of
939 Mississippi Valley-type deposits. Mineral deposits, 28, 195-210. (In
940 Chinese with English abstract).
941 Zhang, G.W., Guo, A.L., Wang, Y.J., Li, S.Z., Dong, Y.P., Liu, S.F., He, D.F.,
942 Cheng, S.Y., Lu, R.K., Yao, A.P. (2013) Tectonics of South China
943 continent and its implications. Science China Earth Sciences, 56,
944 1804-1828.
945 Zhang, S.B., Zheng, Y.F., Wu, Y.B., Zhao, Z.F., Gao, S., Wu, F.Y. (2006) Zircon
946 U-Pb age and Hf-O isotope evidence for Paleoproterozoic metamorphic

947 event in South China. Precambrian Research, 151, 265-288.
948 Zhang, Y.X., Wu, Y., Tian, G., Shen, L., Zhou, Y.M., Dong, W.W., Zeng, R.,
949 Yang, X.C., Zhang, C.Q. (2014) Mineralization Age and the Source of
950 Ore-forming Material at Lehong Pb-Zn Deposit, Yunnan Province:
951 Constraints from Rb-Sr and S Isotopes System. Acta Mineralogica
952 Sinica, 34, 305-311.
953 Zhao, G.C. (2015) Jiangnan Orogen in South China: Developing from
954 divergent double subduction. Gondwana Research, 27, 1173-1180.
955 Zhao, J.H., Zhou, M.F., Yan, D.P., Zheng, J.P., Li, J.W. (2011) Reappraisal of
956 the ages of Neoproterozoic strata in South China: No connection with
957 the Grenvillian orogeny. Geology, 39, 299-302.
958 Zhao, X.F., Zhou, M.F., Li, J.W., Sun, M., Gao, J.F., Sun, W.H., Yang, J.H.
959 (2010) Late Paleoproterozoic to early Mesoproterozoic Dongchuan
960 Group in Yunnan, SW China: Implications for tectonic evolution of the
961 Yangtze Block. Precambrian Research, 182, 57-69.
962 Zhou, J.C., Wang, X.L., Qiu, J.S. (2009) Geochronology of Neoproterozoic
963 mafic rocks and sandstones from northeastern Guizhou, South China:
964 Coeval arc magmatism and sedimentation. Precambrian Research, 170,
965 27-42.
966 Zhou, J.X., Bai, J.H., Huang, Z.L., Zhu, D., Yan, Z.F., Lv, Z.C. (2015) Geology,
967 isotope geochemistry and geochronology of the Jinshachang

carbonate-hosted Pb–Zn deposit, southwest China. Journal of Asian Earth Sciences, 98, 272-284.

Zheng, X.Z. (2012) Geological features and genesis ofWusihe Pb-Zn deposit, Sichuan. MSc Thesis, Chang'an University, Xi'an, China, p. 66 (in Chinese with English abstract).

Zhou, J.X., Luo, K., Wang, X.C., Wilde, S.A., Wu, T., Huang, Z.L., Cui, Y.L., Zhao, J.X. (2018a) Ore genesis of the Fule Pb-Zn deposit and its relationship with the Emeishan Large Igneous Province: Evidence from mineralogy, bulk C-O-S and in situ S-Pb isotopes. Gondwana Research, 54, 161-179.

Zhou, J.X., Huang, Z.L., Yan, Z.F. (2013a) The origin of the Maozu carbonate-hosted Pb-Zn deposit, southwest China: Constrained by C-O-S-Pb isotopic compositions and Sm-Nd isotopic age. Journal of Asian Earth Sciences, 73, 39-47.

Zhou, J.X., Huang, Z.L., Zhou, M., Li, X., Jin, Z.G. (2013b) Constraints of C-O-S-Pb isotope compositions and Rb-Sr isotopic age on the origin of the Tianqiao carbonate-hosted Pb-Zn deposit, SW China. Ore Geology Reviews, 53, 77-92.

Zhou, J.X., Xiang, Z.Z., Zhou, M.F., Feng, Y.X., Luo, K., Huang, Z.L., Wu, T. (2018c) The giant Upper Yangtze Pb-Zn province in SW China: Reviews, new advances and a new genetic model. Journal of Asian

Earth Sciences, 154, 280-315.

Zhou, J.X., Wang, X.C., Wilde, S.A., Luo, K., Huang, Z.L., Wu, T., Jin, Z.G. (2018b) New insights into the metallogeny of MVT Zn-Pb deposits: A case study from the Nayongzhi in South China, using field data, fluid compositions, and in situ S-Pb isotopes. American Mineralogist, 103, 91-108.

Zhou, M.F., Ma, Y.X., Yan, D.P., Xia, X.P., Zhao, J.H., Sun, M. (2006) The Yanbian terrane (Southern Sichuan Province, SW China): A neoproterozoic are assemblage in the western margin of the Yangtze block. Precambrian Research, 144, 19-38.

Zhou, M.F., Yan, D.P., Kennedy, A.K., Li, Y.Q., Ding, J. (2002) SHRIMP U-Pb zircon geochronological and geochemical evidence for Neoproterozoic arc-magmatism along the western margin of the Yangtze Block, South China. Earth and Planetary Science Letters, 196, 51-67.

Zhu, C.W., Liao, S.L., Wang, W., Zhang, Y.X., Yang, T., Fan, H.F., Wen, H.J. (2018) Variations in Zn and S isotope chemistry of sedimentary sphalerite, Wusihe Zn-Pb deposit, Sichuan Province, China. Ore Geology Reviews, 95, 639-648.

Zou, C.N., Dong, D.Z., Wang, S.J., Li, J.Z., Li, X.J., Wang, Y.M., Li, D.H., Cheng, K.M. (2010) Geological characteristics and resource potential of shale gas in China. Petroleum exploration and development, 37,

1010 641-653.

Figure captions

FIGURE 1. (a) Tectonic map of South China. The green dashed box (top left) indicates area shown in (b) (modified from Zhou et al. 2018b). Abbreviations: NCC=North China Craton, QDOB = Qinling-Dabie Orogenic Belt, YB=Yangtze Block, JOB=Jiangnan Orogenic Belt, CB=Cathaysian Block, SGFB=Songpan Ganzê Fold Belt, YA=Yidun Arc, SOB=Sanjiang Orogenic Belt. (b) Simplified tectonic map of the Yangtze block and adjacent orogenic belts with metamorphic complexes, showing distribution of MVT deposits surrounding the Yangtze Block (modified from Zhang et al. 2013; Li et al. 2018). The figure also shows I, the Lower Yangtze northern margin; II, the Tongbai-Dabie southern margin; III, Wudang-Dabashan; IV, Hannan-Micang multi-phased composite basin-mountain foreland deformation systems; V, the Longmenshan intracontinental orogen foreland; VI, the Chuxiong foreland basin, and VII, the Qiandong-Xiangxi-E'xi orogen foreland. The black dashed box (bottom left) indicates the location of the Upper Yangtze Pb-Zn metallogenic province.

FIGURE 2. (a) Geological map of the Wusihe district, showing the sampling area. (b) Cross-section through the Wusihe district, based on drill core logging and geological mapping (modified after Lin (2005)). (c) Schematic stratigraphic column of the Wusihe deposit (modified from Lin (2005)). Legend colors are consistent with Figure 2a. Abbreviations: P=Phosphate, Si=Siliceous.

1032

1033 FIGURE 3. Hand specimen photographs showing different types of ores in the
1034 Wusihe deposit: (a) lamellar ores. (b-f) disseminated ores. (g-h) stockwork
1035 ores. (i-j) brecciated ores. (k-l) massive ores.

1036

1037 FIGURE 4. Photomicrographs in reflected light showing representative
1038 textures of mineral associations from different mineralization stages. (a) Late
1039 stage-III calcite (Cal-III) infilling vugs within Sp-II and Py-I. (b) Sp-II coexisting
1040 with Gn-II, replaced by late Py-III. (c) The late Q-IV veinlets with comb
1041 structure. (d) Brown-red Sp-II, Cal-II and Q-II infilling black shale. (e) Yellow
1042 colloform Sp-II enclosing a brown core. (f) Oscillatory zoned Sp-II showing
1043 periodic color variations. (g) Mosaic Sp-II crystals in siliceous dolostone. (h)
1044 Gn-III coexisting with Sp-III. (i) Gn-III enclosing sphalerite. (j) Late Q-IV and
1045 Cal-IV enclosing Gn-II, infilling Sp-II aggregates. (k) Stock-work ore, showing
1046 Sp-II coexisting with bitumen (Bit). (l) Late Cal-IV and Bit-IV infilling siliceous
1047 dolostone. Abbreviations: Cal=Calcite, Sp=Sphalerite, Py=Pyrite, Gn=Galena,
1048 Q=Quartz.

1049

1050 FIGURE 5. Back scattered images. (a) Diagenetic pyrite (Py) dispersed in
1051 siliceous dolostone. (b) Fine-grained euhedral-subhedral quartz (Q1) enclosed
1052 by galena (Gn-III). (c, d) Coarse-grained euhedral quartz (Q2) coexisting with

dolomite (Dol-II), Gn-II and sphalerite (Sp-II). (e) Late anhedral quartz (Q3) occurs in veinlets infilling fractures of Gn-II and Dol-II. (f) Q3 occurs in veinlets infilling fractures of Sp-II. (g) Py-III replaced the organic matter within the original structure. (h) Disseminated autogenetic K-feldspar (Kf) in dolostone enclosed by sphalerite ore. (i) The image of energy spectra of Kf at *EDS spot 1 (c)*, examined by Energy Dispersive Spectroscopy (EDS). (j-k) Photomosaic of a sphalerite-bearing quartz. SEM-CL image shows textual relationships of Q1-Q3 quartz crystals. Q1 is black euhedral-subhedral quartz. Q2 is later brighter quartz enclosing Q1. Q3 grew into open space, particularly along the margin of sphalerite (black mineral in upper left corner). Q3 cuts both Q1 and Q2. Red circles mark laser ablation spots of 40μm in diameter.

FIGURE 6. Schematic summary of mineral paragenesis in the Wusihe deposit. Four stages of hydrothermal mineralization include stage I (pyrite-sphalerite), stage II (sphalerite-galena), stage III (galena) and stage IV (bitumen-calcite).

FIGURE 7. Concentrations of Li, Na, K and Ge vs. Al (ppm) in quartz from the Wusihe deposit. Reasonable linear correlations on plots of Li, Na and K vs. Al (ppm) are shown by the quartz data, Li vs. Al (R^2 = 0.7129), Na vs. Al (R^2 = 0.6550) and K vs. Al (R^2 = 0.3867), suggesting that compensated substitution mode ($Al^{3+}+H^+/Li^+/Na^+/K^+ \rightarrow Si^{4+}$) governing the incorporation of quartz trace

elements at Wusihe. No clear linear correlation is observed on a plot of Ge vs. Al, indicating that single substitution mode ($Ge^{4+} \rightarrow Si^{4+}$) can be ruled out (Huttenlocher 1935). Al concentrations initially show a general increase (blue arrow) from Q1 to Q2, and then to become more depleted (red arrow) in Q3. This trend suggests the variations of Al solubility in the hydrothermal fluid and indicates the role of acid-producing process resulted from sulfide precipitation, and acid consumption by carbonate buffering.

FIGURE 8. Histogram showing sulfur isotope compositions of sulfide minerals. (a) Bulk sulfur isotopic results. (c) In situ sulfur isotopic compositions. In situ $\delta^{34}S$ values measured in this study span an overall larger range compared to bulk $\delta^{34}S$ values.

FIGURE 9. (a) Distribution pattern of $\delta^{34}S$ values for H_2S and sulfide minerals when sulfate of $\delta^{34}S$ = 33.5‰ (average value of $\delta^{34}S$ values of marine barites within the Ediacaran strata in the Upper Yangtze Pb-Zn metallogenic province; e.g. Zhou et al. 2015, 2018c; Kong et al. 2017; Yuan et al. 2017) is reduced by various mechanisms (modified after Ohmoto and Rye 1979). Yellow shaded area represents in situ $\delta^{34}S$ sulfide values in the Wusihe deposit. TDO-Thermal degradation of organic matter. (b) Distribution of bulk $\delta^{34}S$ values of different color and types of ores in the Wusihe deposit. (c)

Distribution of in situ $\delta^{34}S$ values of different color and types of ores in the Wusihe deposit. Results clearly show that microscale $\delta^{34}S$ values increase from core to rim.

FIGURE 10. Photomicrographs of pyrite and sphalerite from the Wusihe deposit, also showing $\delta^{34}S$ values for spots analyzed by NanoSIMS. (a-d) Photomicrographs of samples: a) Pyrites occurring in the siliceous dolostones are characterized by fine-grained (<1mm) euhedral textures; b) Abundant fine-grained lamellar pyrite. Thicker organic-rich layers often contain more pyrite; c) Pyrite and sphalerite are characterized by fine-grained (<1mm) subhedral to anhedral textures; d) Fine- to coarse-grained massive galena, sphalerite and pyrite aggregates. (e-h) Areas selected for in situ S isotope analysis show homogeneous trace element compositions (for example, ^{34}S, ^{75}As, ^{80}Se, $^{208}Pb^{32}S$); (i-l) Photomicrographs showing variation in $\delta^{34}S$ values of sulfide grains from WSH-07, WSH-36, WSH-23 and WSH-20, respectively. Sample numbers correspond to those listed in Table 1. Abbreviations: Py=pyrite, Sp=sphalerite, OM=organic matter.

FIGURE 11. (a) Comparison plot of Pb isotope ratios $^{207}Pb/^{204}Pb$ vs. $^{206}Pb/^{204}Pb$ among the Wusihe deposit, late Ediacaran Dengying Fm., dolostone, Devonian to Permian carbonate rocks, Proterozoic basement

(Kunyang/Huili Group) and late Permian Emeishan basalts (Huang 2004). Data for Upper Continental Crust (U), Orogen Belt (O), Mantle (M) and Lower Continental Crust (L) are from Zartman and Doe (1981). (b, c) Plots of $^{207}Pb/^{204}Pb$ vs. $^{206}Pb/^{204}Pb$, $^{208}Pb/^{204}Pb$ vs. $^{206}Pb/^{204}Pb$ for galena formed during stage-II (disseminated, brecciated, stockwork) and -III (massive). (d) Comparison plot of $^{207}Pb/^{204}Pb$ vs. $^{206}Pb/^{204}Pb$ of in situ data among the Maliping (MLP), Nayongzhi (NYZ), Yinchanggou (YCG), Wusihe (WSH), and Huize (HZ), Fule (FL), (Liangyan) LY, Maozhachang (MZC) deposits (data from Bao et al. 2017; Tan et al. 2017; Zhou et al. 2018a, b, c and Luo et al. 2019). Letters in brackets represent corresponding sequences hosting the Pb-Zn deposits: *E* = Ediacaran, ϵ = Cambrian, *D* = Devonian, *C* = Carboniferous, *P* = Permian. Dashed lines represent ages. The data imply that ore formation ages clearly fall into two clusters: 1. Maliping, Wusihe and Yinchanggou (black lines) and 2. Nayongzhi, Huize, Liangyan, Maozhachang and Fule (white lines).

FIGURE 12. (a) The ideal model for the evolution of the hydrothermal system in Wusihe, showing metal leaching, fluid mixing, local sulfate reduction and involvement of black shales and carbonate sequences etc. and (b) Schematic section showing the deposition of the ores in Wusihe, showing the spatial relationship between wall rock sequences and different stages of mineralization (modified from Wang et al. 2015).

This is a preprint, the final version is subject to change, of the American Mineralogist (MSA)
Cite as Authors (Year) Title. American Mineralogist, in press.
DOI: https://doi.org/10.2138/am-2020-7021

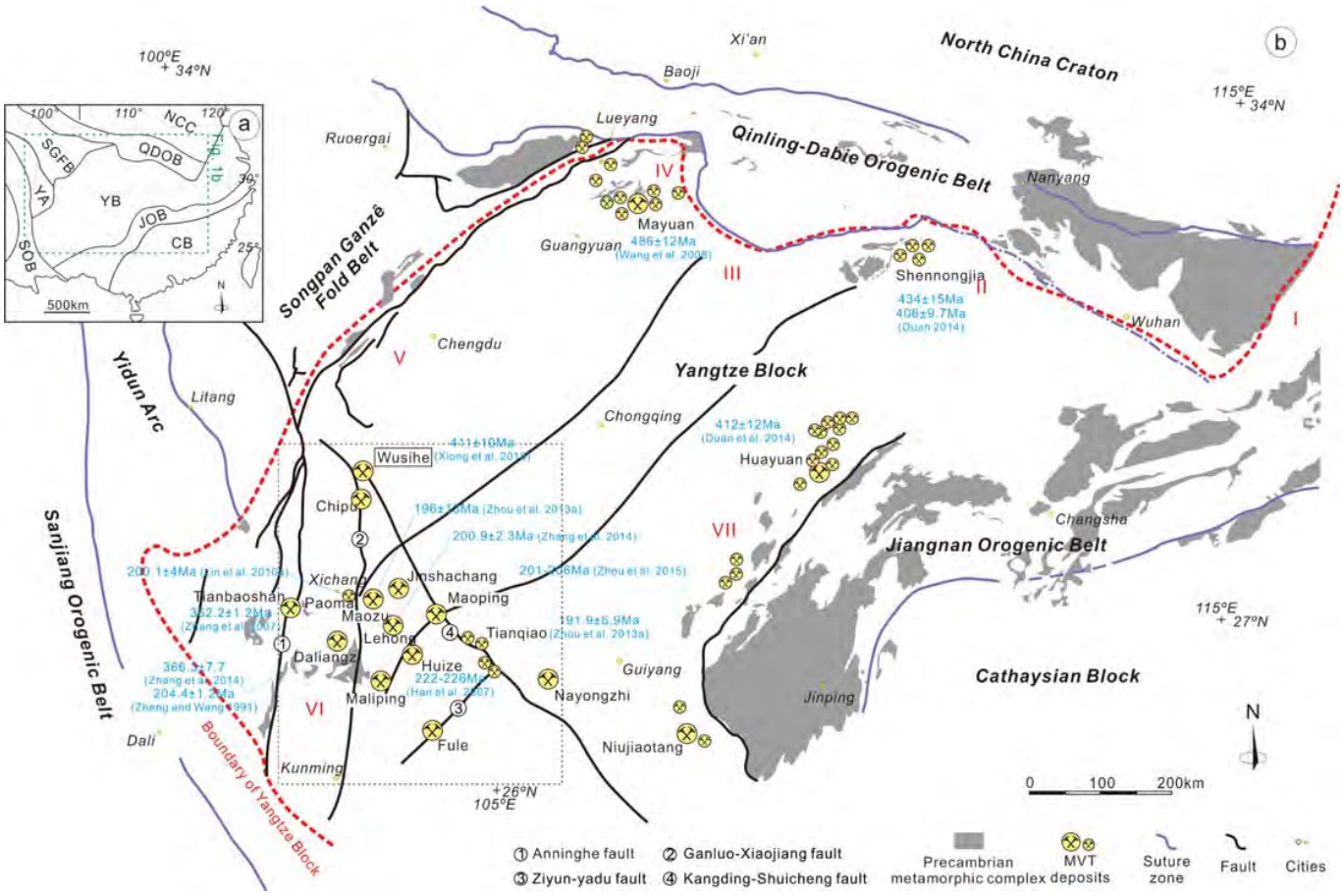

Figure 1

This is a preprint, the final version is subject to change, of the American Mineralogist (MSA)
Cite as Authors (Year) Title. American Mineralogist, in press.
DOI: https://doi.org/10.2138/am-2020-7021

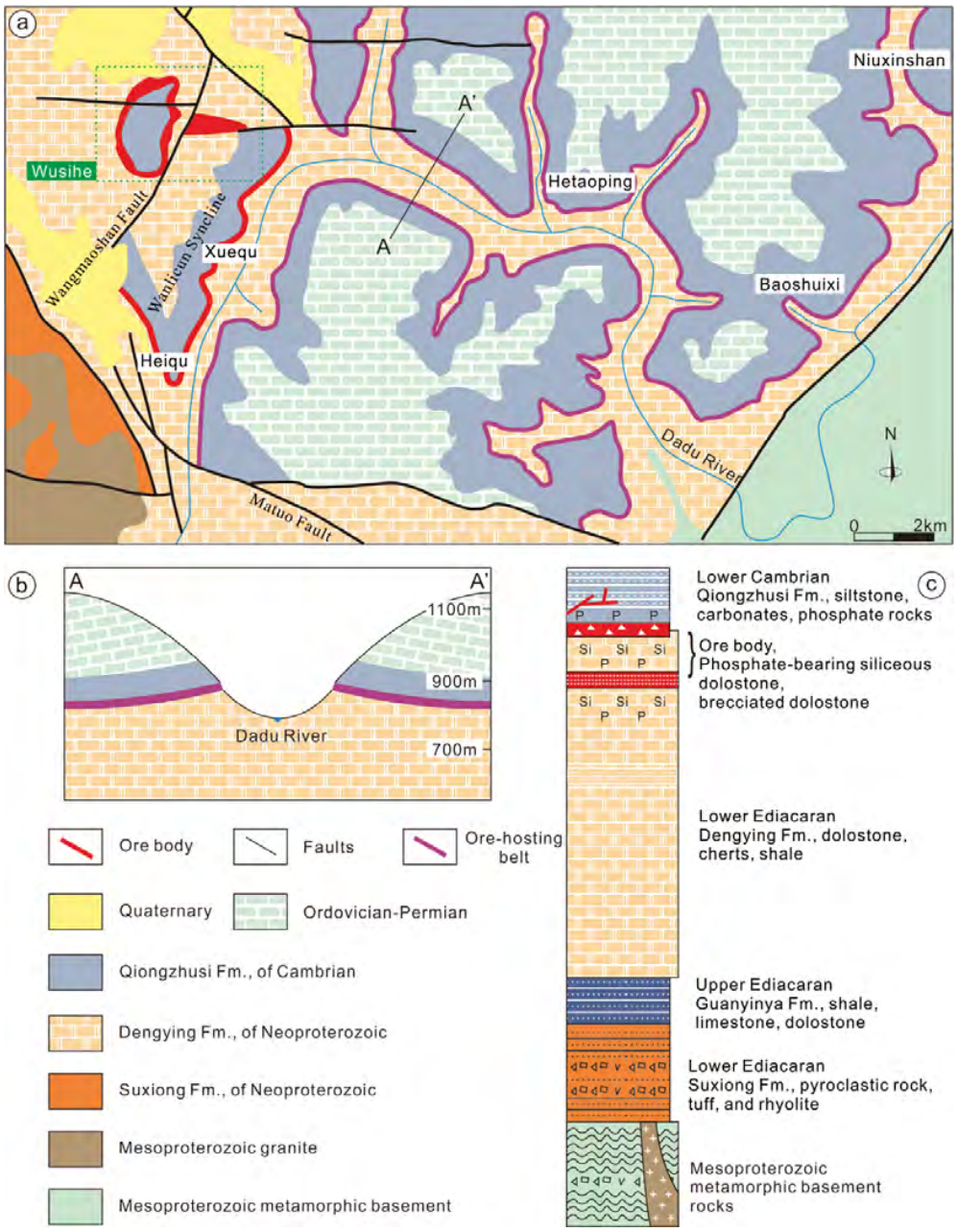

Figure 2

This is a preprint, the final version is subject to change, of the American Mineralogist (MSA)
Cite as Authors (Year) Title. American Mineralogist, in press.
DOI: https://doi.org/10.2138/am-2020-7021

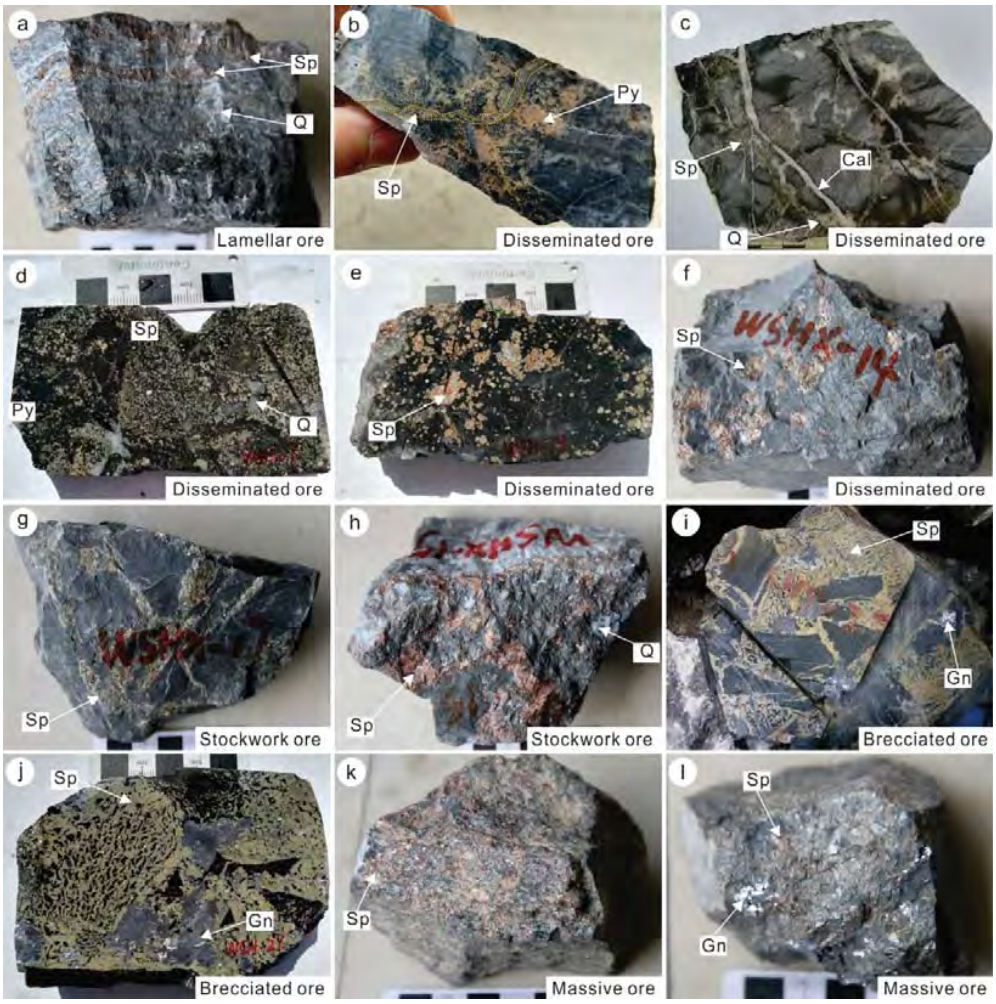

Figure 3

This is a preprint, the final version is subject to change, of the American Mineralogist (MSA)
Cite as Authors (Year) Title. American Mineralogist, in press.
DOI: https://doi.org/10.2138/am-2020-7021

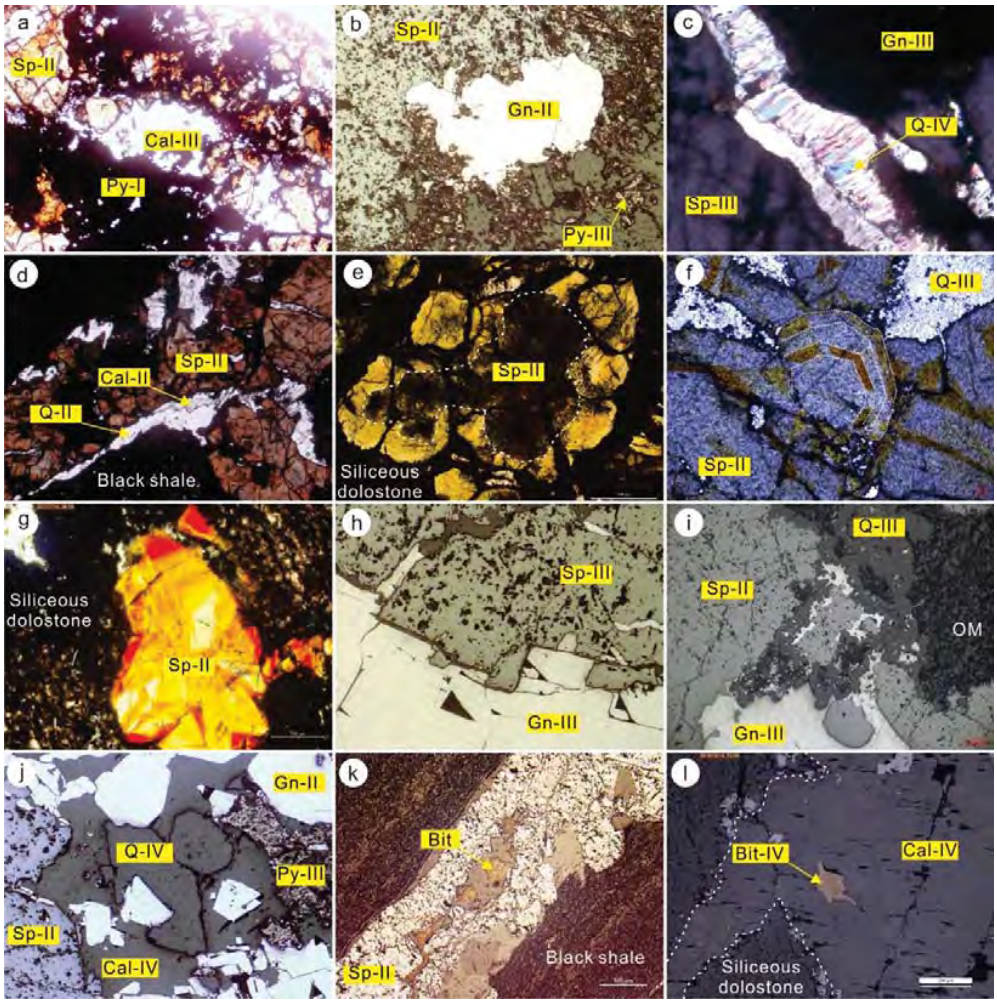

Figure 4

This is a preprint, the final version is subject to change, of the American Mineralogist (MSA)
Cite as Authors (Year) Title. American Mineralogist, in press.
DOI: https://doi.org/10.2138/am-2020-7021

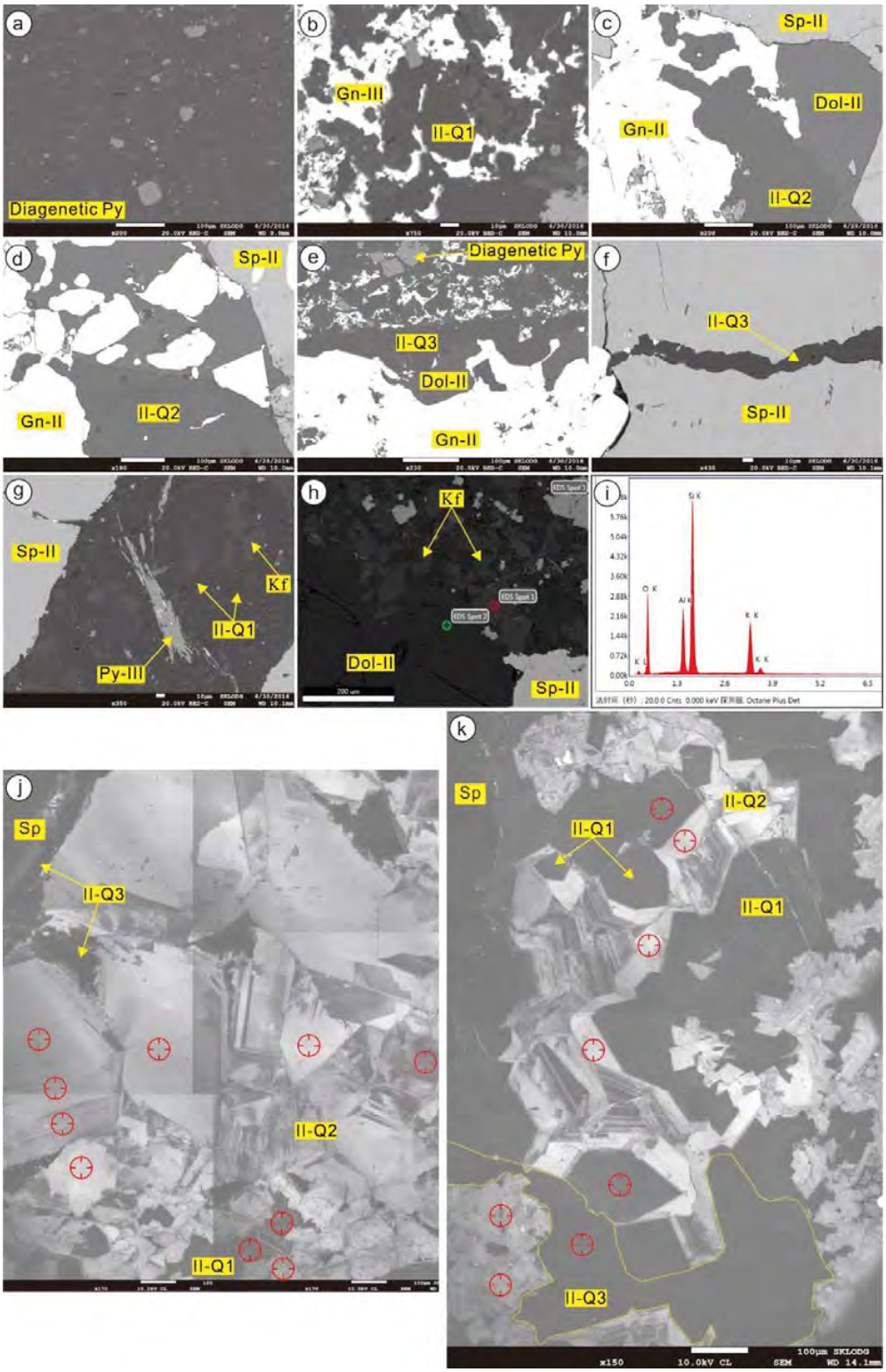

Figure 5

This is a preprint, the final version is subject to change, of the American Mineralogist (MSA)
Cite as Authors (Year) Title. American Mineralogist, in press.
DOI: https://doi.org/10.2138/am-2020-7021

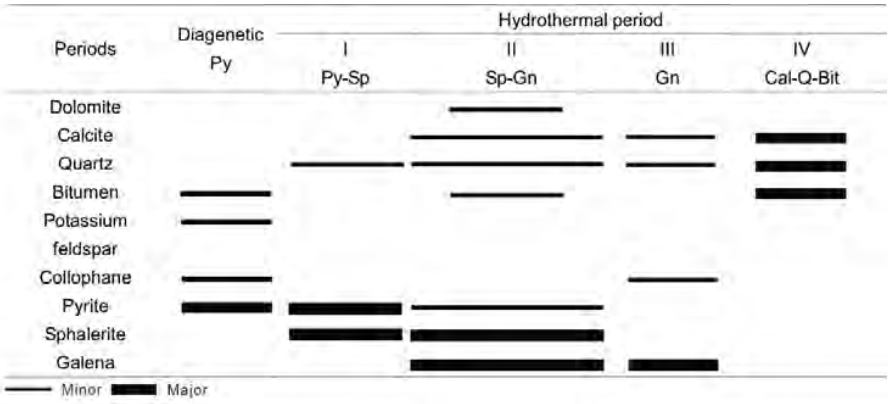

Figure 6

This is a preprint, the final version is subject to change, of the American Mineralogist (MSA)
Cite as Authors (Year) Title. American Mineralogist, in press.
DOI: https://doi.org/10.2138/am-2020-7021

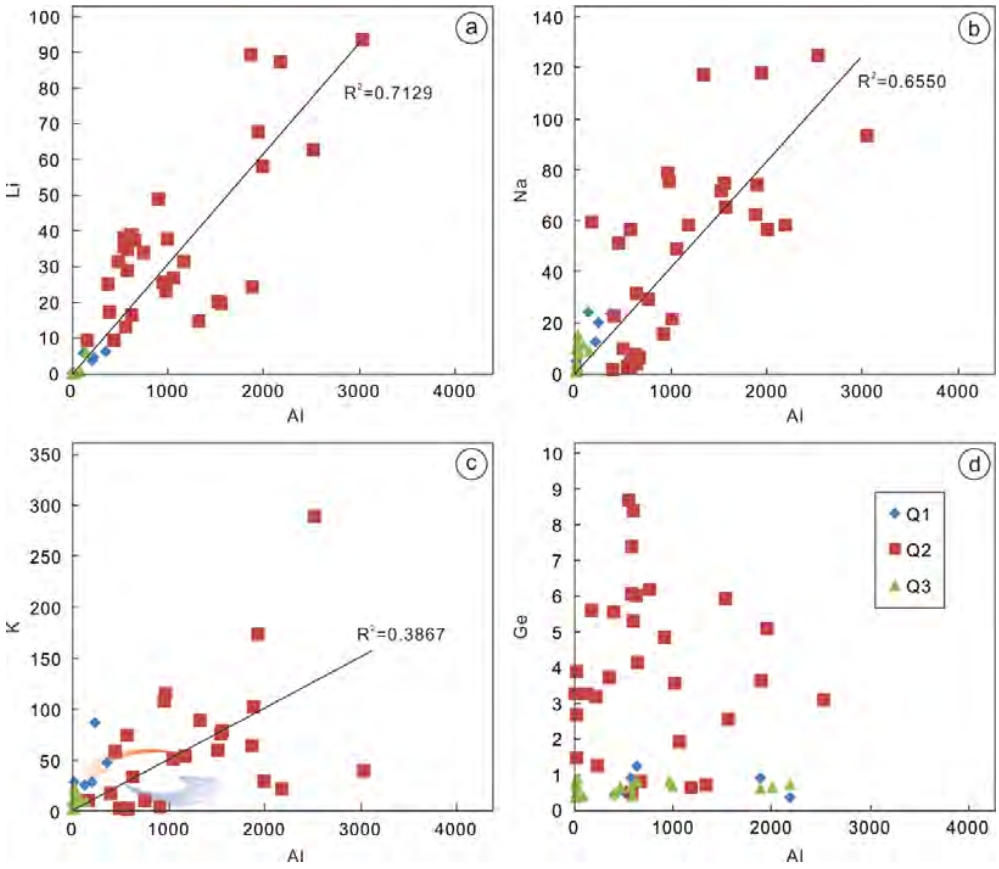

Figure 7

This is a preprint, the final version is subject to change, of the American Mineralogist (MSA)
Cite as Authors (Year) Title. American Mineralogist, in press.
DOI: https://doi.org/10.2138/am-2020-7021

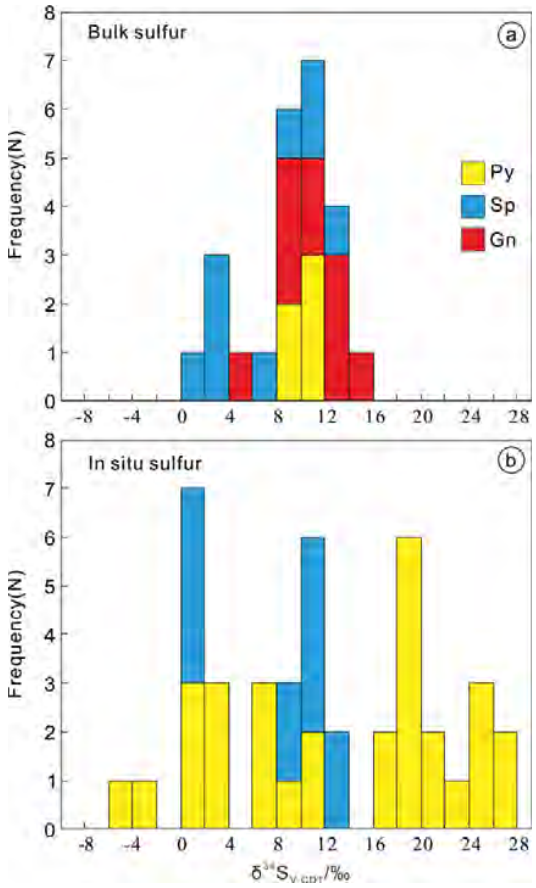

Figure 8

This is a preprint, the final version is subject to change, of the American Mineralogist (MSA)
Cite as Authors (Year) Title. American Mineralogist, in press.
DOI: https://doi.org/10.2138/am-2020-7021

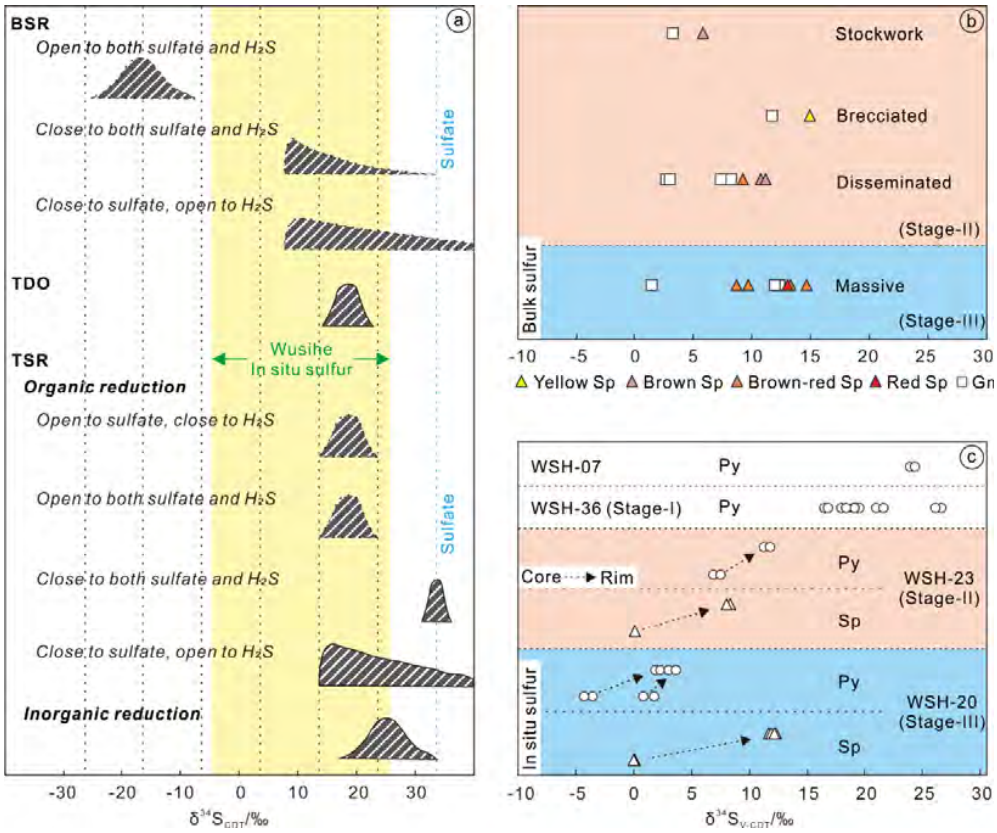

Figure 9

This is a preprint, the final version is subject to change, of the American Mineralogist (MSA)
Cite as Authors (Year) Title. American Mineralogist, in press.
DOI: https://doi.org/10.2138/am-2020-7021

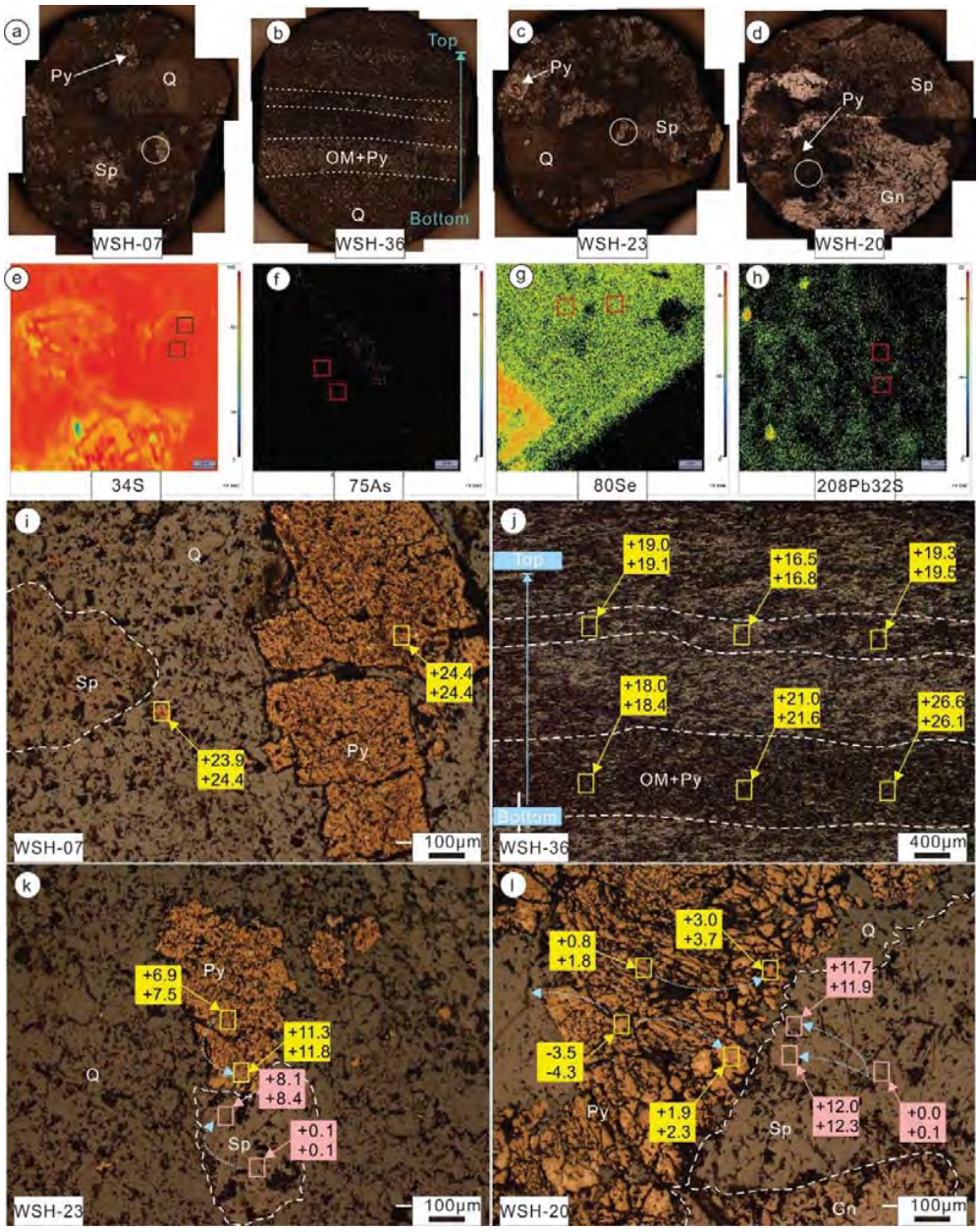

Figure 10

This is a preprint, the final version is subject to change, of the American Mineralogist (MSA)
Cite as Authors (Year) Title. American Mineralogist, in press.
DOI: https://doi.org/10.2138/am-2020-7021

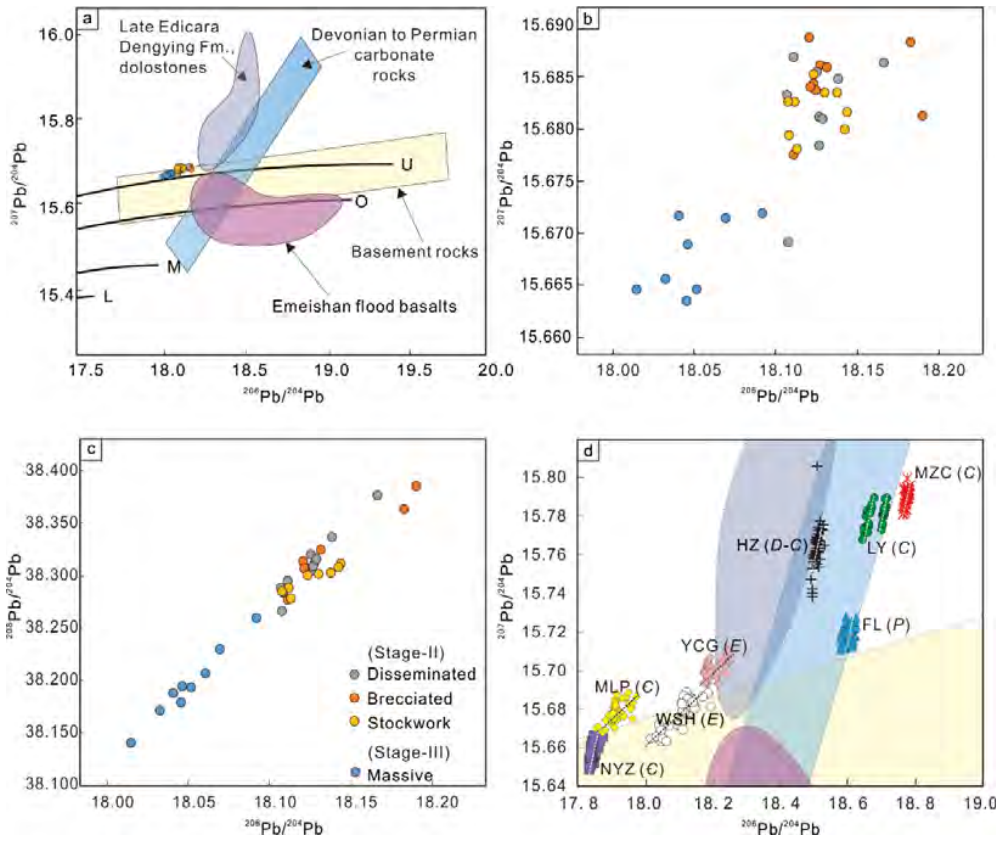

Figure 11

This is a preprint, the final version is subject to change, of the American Mineralogist (MSA)
Cite as Authors (Year) Title. American Mineralogist, in press.
DOI: https://doi.org/10.2138/am-2020-7021

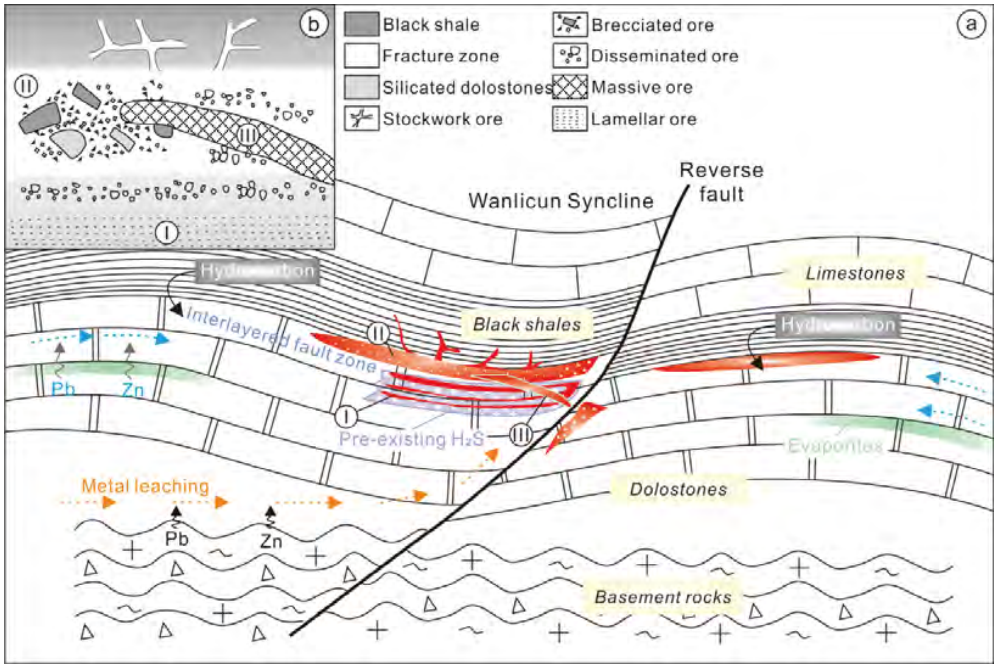

Figure 12

Table 1. Selected trace elements in different generations (II-Q1 -Q3) of quartz from the Wusihe Pb-Zn deposit

Spot name	Generation	CL intensity	Li	Na	Al	K	Ti	Ge
WSH-17-08	Q1	Dark-grey	0.111	5.18	8.46	7.93	0.667	0.368
WSH-17-09	Q1	Dark-grey	0.137	1.59	10.9	5.68	0.461	-
WSH-17-10	Q1	Dark-grey	6.26	23.4	354	48.2	0.848	0.460
WSH-17-36	Q1	Dark-grey	0.153	3.00	25.1	29.0	0.672	0.870
WSH-17-37	Q1	Dark-grey	3.88	12.8	210	28.7	0.479	0.443
WSH-17-38	Q1	Dark-grey	4.79	20.1	234	87.2	9.05	1.20
WSH-17-39	Q1	Dark-grey	0.285	3.07	12.6	8.28	0.831	0.329
WSH-17-40	Q1	Dark-grey	5.67	24.5	122	26.0	1.15	0.870
WSH-1-2	Q2	Light	24.1	73.9	1897	102	1.50	3.23
WSH-1-3	Q2	Dark	20.2	71.7	1532	60.5	1.31	2.62
WSH-1-5	Q2	Dark	19.5	74.7	1563	75.9	0.967	3.69
WSH-1-6	Q2	Dark	14.6	117	1342	89.5	3.40	3.85
WSH-17-1-1	Q2	Light	93.2	92.9	3049	39.8	1.41	3.14
WSH-17-1-3	Q2	Light	48.8	15.3	912	5.04	0.533	1.21
WSH-17-1-4	Q2	Light	37.4	21.3	1012	-	0.385	1.43
WSH-17-1-7	Q2	Grey	31.4	58.3	1180	54.0	1.24	3.22
WSH-17-1-8	Q2	Grey	62.5	125	2529	288	12.3	3.59
WSH-17-2-1	Q2	Light	34.5	2.91	581	1.43	1.22	5.88
WSH-17-2-2	Q2	Light	17.3	22.3	402	17.1	0.349	2.52
WSH-17-2-3	Q2	Light	38.0	7.57	626	-	0.596	0.669
WSH-17-2-4	Q2	Light	33.9	28.7	760	10.4	1.05	-
WSH-17-2-5	Q2	Light	37.3	5.92	668	-	1.28	4.81
WSH-17-2-6	Q2	Light	28.9	6.44	586	3.24	0.816	3.51
WSH-17-2-7	Q2	Light	9.21	59.4	171	10.6	2.52	0.571
WSH-17-2-10	Q2	Light	67.6	118	1949	174	9.20	3.04
WSH-17-19	Q2	Light	37.1	3.83	588	-	1.41	5.99
WSH-17-20	Q2	Light	36.8	3.73	580	-	1.15	5.52
WSH-17-21	Q2	Light	37.0	3.10	582	-	1.51	5.97
WSH-17-22	Q2	Light	35.4	2.80	554	-	1.43	6.14
WSH-17-34	Q2	Light	26.6	48.5	1064	51.3	0.848	0.763
WSH-17-44	Q2	Light	38.8	4.01	635	-	1.23	5.27
WSH-17-45	Q2	Light	36.7	2.95	584	-	1.01	5.54
WSH-17-46	Q2	Light	36.8	2.07	585	-	0.741	5.05
WSH-17-47	Q2	Light	31.3	9.74	501	2.51	0.942	8.34
WSH-17-48	Q2	Light	37.9	1.78	564	-	0.641	0.445
WSH-17-49	Q2	Light	25.1	1.73	389	-	0.805	7.34
WSH-17-50	Q2	Light	38.6	3.62	624	-	1.07	8.65
WSH-17-11	Q2	Light	87.1	58.2	2190	22.5	1.15	1.87
WSH-17-06	Q2	Light	89.3	62.4	1876	63.6	1.70	4.11
WSH-17-07	Q2	Light	58.0	56.6	2002	28.5	0.949	1.17
WSH-1-1	Q2	Light	19.7	64.8	1566	79.1	1.43	3.48

WSH-17-1-5	Q2	Light	16.4	31.3	635	33.6	0.484	-
WSH-17-2-8	Q2	Light	25.6	78.4	959	109	0.525	1.51
WSH-17-2-9	Q2	Light	22.9	75.1	986	115	1.47	1.78
WSH-17-13	Q2	Light	13.1	56.3	581	74.5	1.18	1.05
WSH-17-14	Q2	Light	9.27	50.9	456	57.7	1.16	0.619
WSH-1-4	Q3	Dark	0.709	11.4	85.0	13.8	1.07	-
WSH-17-1-2	Q3	Dark	0.285	0.910	8.36	5.85	0.895	-
WSH-17-1-6	Q3	Dark	0.217	2.96	23.4	20.2	0.814	0.629
WSH-17-01	Q3	Dark	-	4.33	6.75	2.30	0.508	0.448
WSH-17-02	Q3	Dark	-	1.70	4.28	-	0.772	0.813
WSH-17-03	Q3	Dark	-	-	6.02	4.06	0.791	0.719
WSH-17-04	Q3	Dark	0.130	-	5.68	5.65	0.654	0.586
WSH-17-05	Q3	Dark	0.173	1.51	11.3	3.42	0.591	0.619
WSH-17-15	Q3	Dark	0.073	1.35	5.08	2.29	0.419	--
WSH-17-16	Q3	Dark	0.130	15.7	10.8	4.97	0.492	-
WSH-17-17	Q3	Dark	0.136	3.30	22.3	25.1	0.597	0.799
WSH-17-18	Q3	Dark	0.207	7.92	20.7	11.0	0.701	0.673
WSH-17-23	Q3	Dark	-	10.5	3.18	3.84	0.720	0.379
WSH-17-24	Q3	Dark	0.072	1.63	16.6	13.7	0.384	0.624
WSH-17-25	Q3	Dark	0.107	2.54	9.11	2.33	0.609	0.361
WSH-17-26	Q3	Dark	0.208	9.20	28.7	18.0	0.783	0.729
WSH-17-28	Q3	Dark	-	1.29	7.05	5.01	0.532	0.864
WSH-17-29	Q3	Dark	0.096	-	6.94	3.80	0.653	-
WSH-17-30	Q3	Dark	0.319	-	12.7	3.16	0.545	0.358
WSH-17-32	Q3	Dark	-	0.774	3.85	3.29	0.628	0.483
WSH-17-33	Q3	Dark	0.224	12.6	23.4	15.0	0.670	0.848
WSH-17-41	Q3	Dark	0.265	3.31	13.0	9.10	0.405	0.624
WSH-17-42	Q3	Dark	0.391	9.38	25.6	14.2	0.868	-
WSH-17-43	Q3	Dark	6.35	9.02	149	10.6	0.705	-

Notes: - = below detection limit

Table 2. Bulk S isotopic composition of sulfides from the Wusihe Pb-Zn deposit

Sample #	Mineral	Texture	Structure (stage) & color	$\delta^{34}S$ (‰)
WSH-27	Gn	Fine-grained	Brecciated (II)	+11.3
WSH-07	Gn	Coarse-grained	Disseminated (II)	+8.0
WSH-16	Gn	Fine-grained	Disseminated (II)	+3.4
WSH-23	Gn	Fine-grained	Disseminated (II)	+2.9
WSH-24	Gn	Coarse-grained	Disseminated (II)	+7.2
WSH-03	Gn	Coarse-grained	Massive (III)	+12.1
WSH-04	Gn	Coarse-grained	Massive (III)	+11.5
WSH-26	Gn	Fine-grained	Massive (III)	+1.8
WSH-22	Gn	Fine-grained	Stock-work (II)	+3.4
WSH-26	Py	Fine-grained	Massive (III)	+8.6
WSH-28	Py	Fine-grained	Massive (III)	+10.9
WSH-30	Py	Coarse-grained	Massive (III)	+10.8
WSH-34	Py	Coarse-grained	Massive (III)	+8.6
WSH-35	Py	Coarse-grained	Massive (III)	+10.5
WSH-27	Sp	Fine-grained	Brecciated (II); Yellow	+14.3
WSH-16	Sp	Fine-grained	Disseminated (II); Brown-red	+9.0
WSH-23	Sp	Fine-grained	Disseminated (II); Brown	+10.8
WSH-24	Sp	Coarse-grained	Disseminated (II); Brown	+10.4
WSH-03	Sp	Coarse-grained	Massive (III); Brown-red	+14.0
WSH-26	Sp	Fine-grained	Massive (III); Brown-red	+8.5
WSH-28	Sp	Fine-grained	Massive (III); Brown-red	+12.7
WSH-34	Sp	Coarse-grained	Massive (III); Red	+9.4
WSH-35	Sp	Coarse-grained	Massive (III); Red	+12.5
WSH-22	Sp	Fine-grained	Stock-work (II) Brown	+5.8

Gn - Galena; Py - Pyrite; Sp - Sphalerite

Table 3. In situ S isotopic composition of sulfides from the Wusihe Pb-Zn deposit

Sample No.; Ore structure (stage)	Mineral	Spot location	Analysis spot	$\delta^{34}S$ (‰)
WSH-07; Fine-grained, disseminated (Diagenetic)	Py		WSH-07-01	+24.4
			WSH-07-02	+24.4
			WSH-07-03	+23.9
			WSH-07-04	+24.4
WSH-36; Fine-grained lamellar (I)	Py		WSH-36-01	+19.3
			WSH-36-02	+19.5
			WSH-36-03	+16.5
			WSH-36-04	+16.8
			WSH-36-05	+19.0
			WSH-36-06	+19.1
			WSH-36-07	+18.0
			WSH-36-08	+18.4
			WSH-36-09	+21.0
			WSH-36-10	+21.6
			WSH-36-11	+26.6
			WSH-36-12	+26.1
WSH-23; Fine-grained, disseminated (II)	Sp	Rim	WSH-23-01	+8.1
		Rim	WSH-23-02	+8.4
		Core	WSH-23-03	+0.1
		Core	WSH-23-04	+0.1
	Py	Rim	WSH-23-09	+11.3
		Rim	WSH-23-10	+11.8
		Core	WSH-23-06	+7.5
		Core	WSH-23-05	+6.9
WSH-20; Coarse-grained, massive (III)	Sp	Rim	WSH-20-01	+12.0
		Rim	WSH-20-02	+12.3
		Rim	WSH-20-03	+11.7
		Rim	WSH-20-04	+11.9
		Core	WSH-20-07	+0.0
		Core	WSH-20-08	+0.1
	Py	Rim	WSH-20-09	+1.9
		Rim	WSH-20-10	+2.3
		Rim	WSH-20-11	+3.0
		Rim	WSH-20-12	+3.7
		Core	WSH-20-13	+0.8
		Core	WSH-20-14	+1.8
		Core	WSH-20-15	-3.5
		Core	WSH-20-16	-4.3

Py - Pyrite; Sp - Sphalerite

This is a preprint, the final version is subject to change, of the American Mineralogist (MSA)
Cite as Authors (Year) Title. American Mineralogist, in press.
DOI: https://doi.org/10.2138/am-2020-7021

Table 4. In situ Pb isotopic ratios of galena from the Wusihe Pb-Zn deposit

Spot name	Ore structure (stage)	$^{208}Pb/^{204}Pb$	1s	$^{207}Pb/^{204}Pb$	1s	$^{206}Pb/^{204}Pb$	1s	Ref.
WSH-27-01	Brecciated (II)	38.28	0.01	15.68	0.01	18.11	0.01	This study
WSH-27-02		38.31	0.01	15.69	0.01	18.13	0.01	
WSH-27-03		38.36	0.01	15.69	0.01	18.18	0.01	
WSH-27-04		38.39	0.01	15.68	0.01	18.19	0.01	
WSH-27-05		38.31	0.01	15.69	0.01	18.12	0.01	
WSH-27-06		38.32	0.01	15.69	0.01	18.13	0.01	
WSH-27-07		38.30	0.01	15.68	0.01	18.12	0.01	
WSH-27-08		38.31	0.01	15.68	0.01	18.13	0.01	
WSH-27-09		38.31	0.01	15.68	0.01	18.12	0.01	
WSH-37-01	Disseminated (II)	38.30	0.01	15.68	0.01	18.13	0.01	
WSH-37-02		38.31	0.01	15.68	0.01	18.13	0.01	
WSH-37-03		38.34	0.01	15.68	0.01	18.14	0.01	
WSH-37-04		38.32	0.01	15.69	0.01	18.13	0.01	
WSH-37-05		38.27	0.01	15.67	0.01	18.11	0.01	
WSH-37-06		38.32	0.01	15.68	0.01	18.13	0.01	
WSH-37-07		38.29	0.01	15.68	0.01	18.11	0.01	
WSH-37-08		38.38	0.01	15.69	0.01	18.17	0.01	
WSH-37-09		38.29	0.01	15.69	0.01	18.11	0.01	
WSH-40-01	Stock-work (II)	38.31	0.01	15.68	0.01	18.14	0.01	
WSH-40-02		38.31	0.01	15.68	0.01	18.14	0.01	
WSH-40-03		38.30	0.01	15.68	0.01	18.13	0.01	
WSH-40-04		38.28	0.01	15.68	0.01	18.11	0.01	
WSH-40-05		38.28	0.01	15.68	0.01	18.11	0.01	
WSH-40-06		38.30	0.01	15.69	0.01	18.12	0.01	

This is a preprint, the final version is subject to change, of the American Mineralogist (MSA)
Cite as Authors (Year) Title. American Mineralogist, in press.
DOI: https://doi.org/10.2138/am-2020-7021

WSH-40-07		38.30	0.01	15.68	0.01	18.14	0.01	
WSH-40-08		38.29	0.01	15.68	0.01	18.11	0.01	
WSH-40-09		38.28	0.01	15.68	0.01	18.11	0.01	
WSH-20-01		38.18	0.01	15.66	0.01	18.05	0.01	
WSH-20-02		38.19	0.01	15.66	0.01	18.05	0.01	
WSH-20-03		38.21	0.01	15.66	0.01	18.06	0.01	
WSH-20-04		38.14	0.01	15.66	0.01	18.02	0.01	
WSH-20-05	Massive (III)	38.26	0.01	15.67	0.01	18.09	0.01	
WSH-20-06		38.23	0.01	15.67	0.01	18.07	0.01	
WSH-20-07		38.19	0.01	15.67	0.01	18.04	0.01	
WSH-20-08		38.19	0.01	15.67	0.01	18.05	0.01	
WSH-20-09		38.17	0.01	15.67	0.01	18.03	0.01	
Maliping		37.95-38.10		15.67-15.69		17.86-17.97		Luo et al. 2019
Nayongzhi		37.92-37.97		15.65-15.67		17.83-17.84		Zhou et al. 2018b
Yinchanggou		38.51-38.63		15.69-15.71		18.17-18.24		Tan et al. 2017
Huize		38.91-39.08		15.74.15.81		18.49-18.53		Bao et al. 2017
Maozhachang		38.41-38.48		15.78-15.80		18.76-18.76		Zhou et al. 2018c
Liangyan		39.23-39.36		15.77-15.79		18.64-18.71		Zhou et al. 2018c
Fule		38.59-38.73		15.71-15.73		18.57-18.62		Zhou et al. 2018a